



Riemann solutions and spacetime discontinuous Galerkin method for linear elastodynamic contact [☆]



Reza Abedi ^{a,b,*}, Robert B. Haber ^b

^a Department of Mechanical, Aerospace & Biomedical Engineering, University of Tennessee Space Institute, 411 B.H. Goethert Parkway, MS 21, Tullahoma, TN 37388, USA

^b Department of Mechanical Science and Engineering, University of Illinois at Urbana-Champaign, 1206 West Green Street, Urbana, IL 61801, USA

ARTICLE INFO

Article history:

Received 26 November 2012

Received in revised form 16 June 2013

Accepted 26 November 2013

Available online 4 December 2013

Keywords:

Contact
Elastodynamics
Friction
Coulomb relation
Riemann solution
Regularization

ABSTRACT

We derive Riemann solutions for stick, slip and separation contact modes in a linear elastic material with an isotropic Coulomb friction relation and explore their numerical implementation. The Riemann solutions preserve the characteristic structure of the underlying elastodynamic system and imply dynamic contact conditions that are distinct from the quasi-static conditions used in some numerical models.

Nonphysical discontinuities in the standard Coulomb model at stick–slip transitions can cause contact-mode chatter in numerical simulations. We restate the Coulomb relation to remove these artificial discontinuities and eliminate the need for algorithmic remedies. Discontinuous response at abrupt separation-to-contact transitions is physically reasonable, and we propose a regularization scheme to address this case. We implement the Riemann contact solutions within an adaptive spacetime discontinuous Galerkin (SDG) code and report numerical results that demonstrate the model's efficacy.

© 2013 Elsevier B.V. All rights reserved.

1. Introduction

Nonlinear and non-smooth response associated with transitions between contact and separation modes and between stick and slip contact modes pose a number of challenges in the numerical analysis of contact mechanics. In this study, we are concerned with dynamic contact mechanics where impact effects, sharp wave fronts, and possible contact-mode instabilities present additional challenges. General reviews on contact mechanics can be found in [1–4], while the monographs [5–7] address computational contact mechanics. The most common numerical techniques for contact include *penalty methods* [8–12], *Lagrange multiplier methods* [13–18], those based on *variational inequalities* [19–22], or some combination of the latter two [23,24]. Each of these presents a different mix of advantages and disadvantages. Penalty methods allow an unpredictable amount of interpenetration and can generate stiff, ill-conditioned systems that might require extremely small time steps for stability [25] or special adaptive tuning of the model parameters [26–28]. Although Lagrange multiplier methods and variational inequalities weakly enforce the impenetrability constraint and friction model, they may increase problem size or introduce a more complex computational framework, and they typically require more expensive implicit solvers.

Some numerical contact models replace the continuum contact theory with a simpler theory restricted to a finite set of discrete points, typically finite element nodes. The impenetrability constraint is only enforced at these points, and the

[☆] Contract/Grant sponsor: NSF; contract/Grant numbers: DMR 03-25939 ITR/AP, OCI 09-48393 EAGER ARRA.

* Corresponding author at: Department of Mechanical, Aerospace & Biomedical Engineering, University of Tennessee Space Institute, 411 B.H. Goethert Parkway, MS 21, Tullahoma, TN 373888, USA. Tel.: +1 931 393 7334; fax: +1 931 393 7557.

E-mail addresses: rabedi@utk.edu (R. Abedi), r-haber@illinois.edu (R.B. Haber).

continuum model for contact tractions is replaced by a simplified model involving concentrated contact forces. This approach is particularly effective for problems with complicated, unknown contact loci, such as those in crashworthiness and metal forming applications [29,30]. However, it is unable to model continuous contact evolution and it cannot incorporate Riemann solutions in dynamic contact models since these involve tractions, rather than forces. Moving-grid contact models based on Eulerian or Arbitrary Lagrangian–Eulerian (ALE) kinematics [31–34] generate high-resolution solutions that demonstrate the advantages of using continuum contact theory and tracking precisely the loci of contact-mode transitions in critical applications where the fine details of contact response are important.

Discontinuous and nonsmooth response across contact-mode transitions presents special challenges to the numerical analyst. In some cases, discontinuous response is intrinsic to the contact physics, but in others it is merely an artifact of the chosen form of the mathematical model. For example, the direction of the sliding velocity determines the direction of the friction traction in Coulomb models for contact–slip conditions. Since the magnitude of the sliding velocity varies continuously in time and vanishes in stick mode, the sliding velocity vector must be zero at stick–slip transitions, and this implies an ambiguous, possibly discontinuous, direction for the limiting value of the slip friction traction. Numerical problems associated with these nonphysical discontinuities, such as mode chatter and nonconvergence, are well known, and various remedies are proposed in the literature [35–38]. On the other hand, tractions and velocities exhibit genuinely discontinuous response across separation-to-contact transitions where dynamic impact generates weak shocks. Suitably robust numerical methods are required to model these events accurately without spurious ringing, Gibbs effects or numerical dissipation.

In this work, we present a reformulation of the continuum elastodynamic contact problem and propose an adaptive spacetime numerical method to address several of the open issues noted above. Certain simplifications and caveats are reasonable in the particular application in dynamic brittle fracture that motivates our research. Accordingly, from here on, we assume macroscopically smooth contact interfaces, linear and isotropic elastic response in the bulk material with possibly distinct materials adjacent to contact interfaces, and a simple isotropic Coulomb friction model with identical static and kinetic friction coefficients. We also assume that the loci of potential contact interfaces are known *a priori*, so we do not address methods for nucleating and evolving contact interfaces. We discuss prospects for relaxing some of these restrictions in 5 to address applications that require a more robust theory and implementation.

We present our continuum formulation in the following section. After reviewing the governing equations for linear elastodynamics, we present Riemann solutions for the complete set of dynamic contact modes in 2.2. Although several of the Riemann solutions are similar to previous results, the Riemann solution for the contact–slip case is new to the best of our knowledge. We present an alternative statement of the isotropic Coulomb friction relation in 2.2.2 that eliminates the nonphysical discontinuities at stick–slip transitions described above as well as the need for algorithmic remedies for the numerical problems they create.

Our Riemann solutions imply contact conditions that are distinct from quasi-static conditions that do not explicitly account for the hyperbolic characteristic structure of the underlying elastodynamic system. They imply preservation of characteristic structure across interfaces. Some models that do not preserve characteristic structure have, nonetheless, been shown to generate accurate contact solutions when suitable algorithmic corrections are applied, *e.g.*, [13]. We demonstrated in [39,40] that enforcing Riemann fluxes at element boundaries generally improves accuracy and eliminates spurious global oscillations in elastodynamics problems with shocks (but no contact) without resorting to dissipative corrections. We expect, and our numerical results confirm, that these benefits extend to dynamic contact problems where impact events can generate weak shocks.

Separation-to-contact transitions are the only ones where a change in contact mode generates genuinely discontinuous physical response in bodies with macroscopically smooth interfaces. We propose a regularization for these transitions in 2.3 that interpolates between the separation and contact Riemann solutions to control overshoot and undershoot and improve numerical convergence. Our regularization scheme limits interpenetration at contact interfaces to a user-specified value, possibly zero, and does not cause ill-conditioning in the system equations.

In 3, we describe an implementation of the new contact model within an adaptive spacetime discontinuous Galerkin (SDG) finite element method [41,39,40,42–44]. This involves direct discretization on a fully unstructured spacetime mesh that we generate adaptively as the solution progresses. There is no need for a separate time-marching scheme because temporal integration of the governing equations is subsumed within the SDG discretization. The use of discontinuous basis functions on suitably constructed grids [45,46] leads to an asynchronous solution procedure with element-wise balance properties, linear computational complexity in the number of spacetime elements, no global constraint on the local time increment, and a natural structure for parallel computation. Critical to the present contact application, the SDG model provides sufficient degrees of freedom at inter-element boundaries and contact interfaces to weakly enforce both the Riemann flux conditions and the jump conditions that derive from momentum balance and kinematic compatibility. Overall, enforcing the contact Riemann solutions ensures satisfaction of both the impenetrability constraint and the friction relation across all contact modes. No additional constraint methodology, such as a Lagrange multiplier or a penalty method, is required.

We present numerical results in 4 to demonstrate our SDG implementation of the Riemann contact conditions. We begin with benchmark problems involving dynamic impact between linearly elastic rods comprised of either similar or dissimilar materials. Our solutions are virtually free of the nonphysical oscillations, contact-mode chatter and numerical dissipation that reveal the limitations of previous numerical contact models. Next, we present numerical results in two spatial dimensions for an impact problem and for high-velocity, unstable contact in a model brake pad and disk system. These solutions demonstrate our model's ability to resolve complex contact-mode transitions and high-frequency, slip–separation waves.

Overall, our results demonstrate the efficacy of the underlying adaptive SDG model and the benefits of replacing quasi-static contact conditions with the Riemann solutions for dynamic conditions proposed in this work.

2. Formulation

This section presents a continuum formulation for linear elastodynamic contact, including Riemann solutions for the various contact and separation modes. The Riemann solutions specify the mathematically and physically correct fluxes, in the form of traction and velocity fields on opposing sides of a contact interface, consistent with the characteristic structure of the underlying elastodynamic system.

Let d denote the spatial dimension. We define the *contact trajectory*, denoted by Γ , as the union of all spacetime d -manifolds in $\mathbb{E}^d \times \mathbb{R}$ where there is either active or imminent contact at every location in the manifold. These manifolds are vertical in the spacetime setting (*i.e.*, parallel to the time axis) as they represent trajectories of material interfaces in the reference configuration. We assume that Γ is sufficiently regular so that a unique spatial normal vector can be computed almost everywhere.

In general, the identification of Γ is an important aspect of a robust contact solution algorithm. However, for simplicity, we assume in this work that Γ is known *a priori*. Since we define Γ to include regions that are only in imminent contact, we must address *separation* as a possible contact mode, in addition to *contact-stick* and *contact-slip*. We describe below a method that determines the contact mode at any given point on Γ .

2.1. Governing equations and characteristic analysis of linear elastodynamics

Fig. 1 shows an arbitrary point P on $\Gamma \subset \mathbb{E}^2 \times \mathbb{R}$ and a local frame with coordinates (ξ_1, ξ_2, t) , in which t denotes time. In the more general setting, $\mathbb{E}^3 \times \mathbb{R}$, there is an additional local spatial coordinate, ξ_3 , and the local spatial coordinates are defined with respect to the ordered basis $(\mathbf{e}_1, \mathbf{e}_2, \mathbf{e}_3)$, in which \mathbf{e}_1 is a unit vector normal to Γ . As detailed in 2.2.5, the following development, with minor modifications, holds for arbitrary spatial dimension d . From here on, we adopt the standard summation convention, with Latin indices ranging from 1 to d . All component expressions from here on are defined with respect to the local frame; standard transformation rules apply for computing components in the global frame.

We develop our solution from the system,

$$\nabla \cdot \mathbf{S} + \rho \mathbf{b} = \dot{\mathbf{p}} \quad (1a)$$

$$\mathbf{S} = \mathbf{C}(\mathbf{E}), \quad \mathbf{p} = \rho \mathbf{g}(\mathbf{v}) \quad (1b)$$

$$\dot{\mathbf{E}} = \frac{1}{2}(\nabla \mathbf{v} + \nabla^T \mathbf{v}), \quad \mathbf{v} = \dot{\mathbf{u}} \quad (1c)$$

where \mathbf{u} , \mathbf{v} , \mathbf{E} , \mathbf{p} , \mathbf{S} , and \mathbf{b} are displacement, velocity, strain, linear momentum density, stress, and body force fields. Eq. (1a) is the familiar equation of motion. The constitutive Eqs. (1b) express the force-like fields as functions of the kinematic fields, the elasticity tensor \mathbf{C} , the mass density ρ , and a metric tensor \mathbf{g} that transforms the covector basis into the vector basis. In the case of orthonormal bases, such as the ones used here, we have the component representation, $\mathbf{g} = \delta^{ij} \mathbf{e}_i \otimes \mathbf{e}_j$, so that (1b) yields $S^{ij} = C^{ijkl} E_{kl}$ and $p^j = \rho \delta^{ij} v_j$. Eq. (1c) are the kinematic compatibility relations that couple the displacement, strain and velocity fields.

We assume isotropic material response for simplicity, so the components of the elasticity tensor reduce to $C^{ijkl} = \lambda \delta^{ij} \delta^{kl} + \mu (\delta^{ik} \delta^{jl} + \delta^{il} \delta^{jk})$, where λ and μ are the Lamé parameters. Thus, we get $S^{ij} = 2\mu \delta^{ik} \delta^{jl} E_{kl} + \lambda \delta^{ij} E_{kk}$. Under these conditions, the system (1) expands to the following system of scalar conservation laws in which the indices refer to the local coordinate frame.

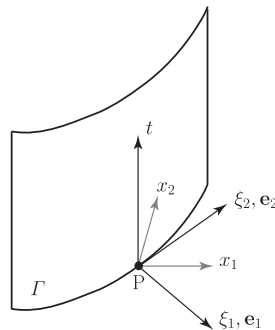


Fig. 1. Local coordinate frame at arbitrary spacetime location P on contact trajectory Γ , an oriented manifold in $\mathbb{E}^2 \times \mathbb{R}$. The local coordinate frame, (ξ_1, ξ_2, t) , is defined such that the ξ_1 -direction aligns with the spatial normal vector on Γ . The local frame is, in general, distinct from the global frame, (x_1, x_2, t) .

$$\begin{aligned}
 \rho v_{1,t} - S_{,1}^{11} - S_{,2}^{12} - S_{,3}^{13} &= \rho b^1 \\
 \rho v_{2,t} - S_{,1}^{12} - S_{,2}^{22} - S_{,3}^{23} &= \rho b^2 \\
 \rho v_{3,t} - S_{,1}^{13} - S_{,2}^{23} - S_{,3}^{33} &= \rho b^3 \\
 S_{,t}^{11} - (\lambda + 2\mu)v_{1,1} - \lambda v_{2,2} - \lambda v_{3,3} &= 0 \\
 S_{,t}^{12} - \mu v_{1,2} - \mu v_{2,1} &= 0 \\
 S_{,t}^{13} - \mu v_{1,3} - \mu v_{3,1} &= 0 \\
 S_{,t}^{22} - \lambda v_{1,1} - (\lambda + 2\mu)v_{2,2} - v_{3,3} &= 0 \\
 S_{,t}^{23} - \mu v_{2,3} - v_{3,2} &= 0 \\
 S_{,t}^{33} - \lambda v_{1,1} - \lambda v_{2,2} - (\lambda + 2\mu)v_{3,3} &= 0
 \end{aligned} \tag{2}$$

These equations can be written as,

$$\mathbf{q}_t + \mathbf{A}_1 \mathbf{q}_{,1} + \mathbf{A}_2 \mathbf{q}_{,2} + \mathbf{A}_3 \mathbf{q}_{,3} = \mathbf{R} \tag{3}$$

in which

$$\mathbf{q} := \begin{bmatrix} v_1 \\ v_2 \\ v_3 \\ S^{11} \\ S^{12} \\ S^{13} \\ S^{22} \\ S^{23} \\ S^{33} \end{bmatrix}, \quad \mathbf{R} := \begin{bmatrix} \rho b^1 \\ \rho b^2 \\ \rho b^3 \\ 0 \\ 0 \\ 0 \\ 0 \\ 0 \\ 0 \end{bmatrix}, \quad \mathbf{A}_1 := - \begin{bmatrix} 0 & 0 & 0 & 1/\rho & 0 & 0 & 0 & 0 & 0 \\ 0 & 0 & 0 & 0 & 1/\rho & 0 & 0 & 0 & 0 \\ 0 & 0 & 0 & 0 & 0 & 1/\rho & 0 & 0 & 0 \\ \lambda + 2\mu & 0 & 0 & 0 & 0 & 0 & 0 & 0 & 0 \\ 0 & \mu & 0 & 0 & 0 & 0 & 0 & 0 & 0 \\ 0 & 0 & \mu & 0 & 0 & 0 & 0 & 0 & 0 \\ \lambda & 0 & 0 & 0 & 0 & 0 & 0 & 0 & 0 \\ 0 & 0 & 0 & 0 & 0 & 0 & 0 & 0 & 0 \\ \lambda & 0 & 0 & 0 & 0 & 0 & 0 & 0 & 0 \end{bmatrix} \tag{4}$$

and matrices \mathbf{A}_2 and \mathbf{A}_3 are defined similarly to \mathbf{A}_1 with appropriate shifts of the nonzero elements.

We seek the Riemann solution to (3) for plane waves propagating in the ξ_1 direction. That is, we consider vanishing body force ($\Rightarrow \mathbf{R} = 0$) with $\mathbf{q}_{,2} = \mathbf{q}_{,3} = 0$ and use the left eigenvalue decomposition of \mathbf{A}_1 to diagonalize the resulting system. Let the rows of matrix \mathbf{U} be the left eigenvectors of \mathbf{A}_1 , and let Λ be the corresponding diagonal matrix of eigenvalues. According to $\mathbf{U}\mathbf{A}_1 = \Lambda\mathbf{U}$, and with $\mathbf{w} := \mathbf{U}\mathbf{q}$, we obtain

$$\mathbf{w}_{,t} + \Lambda \mathbf{w}_{,1} = 0 \iff w_{,t}^\alpha + \lambda_\alpha w_{,1}^\alpha = 0, \quad \alpha = 1, \dots, 9 \tag{5}$$

in which, here and below, we follow a standard indicial notation convention, in which Latin indices range over the coordinate directions, Greek indices cover some other specified range, and no summation is implied when one member of a pair of repeated indices is underlined>. The coefficients λ_α are main diagonal terms of the matrix Λ , not to be confused with the Lamé parameter, λ . Eq. (5) implies that the characteristic values, w_α , are constant along spacetime rays with speeds λ_α . The matrices Λ and \mathbf{U} are given by,

$$\Lambda = \text{diag} \begin{bmatrix} -c_d \\ -c_s \\ -c_s \\ 0 \\ 0 \\ 0 \\ c_s \\ c_s \\ c_d \end{bmatrix}, \quad \mathbf{U} = \begin{bmatrix} \rho c_d & 0 & 0 & 1 & 0 & 0 & 0 & 0 & 0 \\ 0 & \rho c_s & 0 & 0 & 1 & 0 & 0 & 0 & 0 \\ 0 & 0 & \rho c_s & 0 & 0 & 1 & 0 & 0 & 0 \\ 0 & 0 & 0 & 0 & 0 & 0 & 0 & 1 & 0 \\ 0 & 0 & 0 & -\frac{\lambda}{\lambda+2\mu} & 0 & 0 & 1 & 0 & 0 \\ 0 & 0 & 0 & -\frac{\lambda}{\lambda+2\mu} & 0 & 0 & 0 & 0 & 1 \\ 0 & 0 & -\rho c_s & 0 & 0 & 1 & 0 & 0 & 0 \\ 0 & -\rho c_s & 0 & 0 & 1 & 0 & 0 & 0 & 0 \\ -\rho c_d & 0 & 0 & 1 & 0 & 0 & 0 & 0 & 0 \end{bmatrix}, \tag{6}$$

in which c_d and c_s denote the dilatational and shear-wave speeds given by,

$$c_d = \sqrt{\frac{\lambda + 2\mu}{\rho}}, \quad c_s = \sqrt{\frac{\mu}{\rho}}. \tag{7}$$

Fig. 2 depicts the characteristic directions and corresponding eigen and characteristic values at a given point on Γ . For convenience, we have grouped the characteristic values in (6) into three groups according to the direction of wave propagation along the ξ_1 -axis as determined by their corresponding characteristic directions. Quantities associated with waves

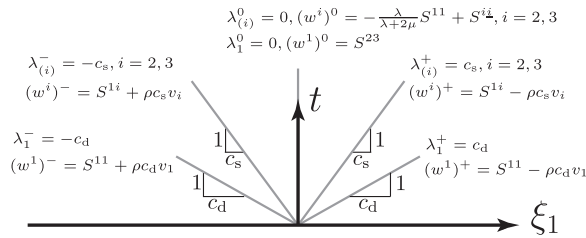


Fig. 2. Characteristic values/directions are grouped according to the direction of wave propagation along the ξ_1 -axis, as indicated by superscripts '+', '-' and '0'. Characteristic values w^i are constant along their corresponding characteristic directions.

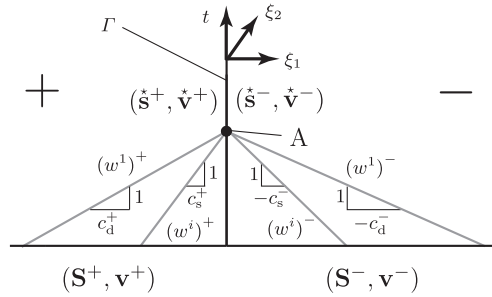


Fig. 3. Riemann problem, projected into the ξ_1 - t plane, for distinct initial data on opposing sides, + and -, of the trajectory Γ of a generic material interface in $2d \times \text{time}$. By convention, the ξ_1 -direction in the local coordinate frame (ξ_i, t) aligns with the outward spatial normal vector for the region on the + side of Γ ; cf. Fig. 1.

traveling in the positive ξ_1 -direction are indicated with a superscript '+', those with waves traveling in the negative ξ_1 -direction with a superscript '-', and those associated with stationary waves with a superscript '0'. The largest positive characteristic value, c_d , corresponds to the wave with longitudinal material motion in the ξ_1 direction, and the repeated characteristic values of c_s correspond to shear waves with transverse material motion in directions tangential to Γ . The characteristic directions on the left side, associated with waves with negative velocities in the ξ_1 -direction, are mirror images of the characteristic directions on the right side. Finally, the three zero characteristic values correspond to stationary waves associated with the stress components S^{23} , S^{22} and S^{33} .

2.2. Riemann solutions for contact and separation

Fig. 3 diagrams the elastodynamic Riemann problem on the trajectory Γ of a generic material interface. The opposing sides, labeled + and -, have distinct initial data, \mathbf{S}^\pm and \mathbf{v}^\pm , and material data, ρ^\pm , λ^\pm and μ^\pm . By convention, the + side is the one whose outward spatial normal vector on Γ aligns with the ξ_1 -direction, so that the set of characteristics denoted with superscript + flow outward. Although this choice of orientation on Γ is arbitrary, we emphasize that, provided all tensor components are expressed consistently with respect to the local frame, the component expressions in the following development are valid and independent of the chosen orientation.

We seek the Riemann values at point A on Γ and denote these quantities with a superposed star. The Riemann values include the traction vector acting on Γ at A,

$$\star \mathbf{s} := \mathbf{S}^t(\mathbf{e}_1) \iff \star s^i := S^{ti} \tag{8}$$

and the velocity vector, $\star \mathbf{v}$.¹ Herein, \mathbf{S}^t denotes the transpose of the stress tensor. In general, distinct Riemann values might arise on Γ due to the distinct initial data on its two sides; we distinguish these Riemann values with superscripts + and -.

The Riemann values are governed by the characteristic structure of the underlying hyperbolic system and constrained by jump conditions that derive from balance of linear momentum and kinematic compatibility. In the absence of external actions on Γ , balance of linear momentum requires equality between the traction vectors generated on Γ by the traces of the stress fields from its opposing sides. That is,

$$\llbracket \star \mathbf{s} \rrbracket = \mathbf{0} \iff \star \mathbf{s}^+ = \star \mathbf{s}^- \text{ on } \Gamma, \tag{9}$$

¹ In [47] we demonstrate that these Riemann quantities correspond to the restrictions of spacetime differential forms called the spacetime linear momentum flux and the strain-velocity to a material spacetime manifold, such as Γ .

where $\llbracket f \rrbracket := f^- - f^+$ is the jump operator across Γ in which f^\pm denote values of f computed from the data on its opposing sides, cf. Fig. 3. The orientation at any point on Γ is unique, so we use the same normal vector, \mathbf{e}_1 , in (8) to extract the tractions \mathbf{s}^\pm .

The form of the jump condition for kinematic compatibility on Γ depends on whether the material interface is perfectly bonded, or in the case of contact, on the specific contact mode (stick or slip). In the cases of perfectly bonded interfaces and contact–stick, the kinematic jump condition for velocity enforces continuity of all velocity components. In contact–slip mode, the jump condition enforces continuity of only the normal velocity component, v_1 , while v_i^+ and v_i^- are independent for $i = 2, 3$. For values of i where v_i is continuous, the velocity jump condition for contact takes the form,

$$\llbracket v_i \rrbracket = 0 \iff \check{v}_i^+ = \check{v}_i^-. \tag{10}$$

For the remaining values of i , if any, v_i^+ and v_i^- are independent. No velocity jump condition is enforced in separation mode, where \mathbf{v}^+ and \mathbf{v}^- are independent.

We use a characteristic analysis of the governing equations subject to (9) and (10) to determine the Riemann values on Γ , denoted by $\check{\mathbf{s}}$ and $\check{\mathbf{v}}$. The characteristic velocities for dilatational waves traveling parallel to the ξ_1 -direction across Γ are $\pm c_d \mathbf{e}_1$. For shear waves involving tangential motion in directions 2 and 3, the characteristic velocities are $\pm c_s \mathbf{e}_1$. For the sake of compactness, we combine these relations in a single statement, $(c^i)^\pm := (c^i)^\pm \mathbf{e}_1$, in which

$$(c^i)^\pm = \begin{cases} \pm c_d & i = 1 \\ \pm c_s & i = 2, 3 \end{cases}. \tag{11}$$

For linear elastodynamics and our assumed isotropic material, the characteristic values are $(w^i)^\pm = (s^i - \rho c^i v_i)^\pm$. Since these are preserved along characteristic rays on each side of Γ , we have

$$(w^i)^\pm|_A = \check{s}^i - (\rho c^i \check{v}_i)^\pm, \tag{12}$$

in which we have used (9) to replace $(\check{s}^i)^\pm$ with the common value, \check{s}^i ; cf. Fig. 2. We specialize (12) below to derive Riemann solutions for specific contact modes using the applicable forms of the velocity jump conditions (10).

2.2.1. Trial Riemann solution for assumed contact–stick conditions

We next derive a trial Riemann solution, denoted by $(\check{\mathbf{s}}, \check{\mathbf{v}})$, for assumed contact–stick conditions. We use the trial solution in the subsequent development to test whether separation or contact conditions hold and, if the latter, whether the contact mode is stick or slip. We denote contact–slip Riemann solutions with $(\check{\mathbf{s}}, \check{\mathbf{v}})$, active contact Riemann solutions, whether they are in slip or stick mode, with $(\check{\mathbf{s}}, \check{\mathbf{v}})$, and separation Riemann solutions with $(\check{\mathbf{s}}, \check{\mathbf{v}})$.

We assume that Γ is in contact–stick mode to begin the formulation of the trial solution, $(\check{\mathbf{s}}, \check{\mathbf{v}})$. Under this assumption, (10) holds for all values of i and, when combined with (12), yields the system,

$$(w^i)^\pm|_A = \check{s}^i - (\rho c^i)^\pm \check{v}_i. \tag{13}$$

Solving (13) for the trial Riemann values, we obtain (no sum on i)

$$\check{s}^i = \frac{\llbracket w^i / \rho c^i \rrbracket}{\llbracket (\rho c^i)^{-1} \rrbracket} = \frac{\llbracket s^i / \rho c^i \rrbracket - \llbracket v_i \rrbracket}{\llbracket (\rho c^i)^{-1} \rrbracket} \tag{14a}$$

$$\check{v}_i = -\frac{\llbracket w^i \rrbracket}{\llbracket \rho c^i \rrbracket} = \frac{-\llbracket s^i \rrbracket + \llbracket \rho c^i v_i \rrbracket}{\llbracket \rho c^i \rrbracket}. \tag{14b}$$

The expanded forms of (14) for the normal Riemann values are

$$\check{s}^1 = \frac{(w^1)^+(\rho c_d)^- + (w^1)^-(\rho c_d)^+}{(\rho c_d)^+ + (\rho c_d)^-} = \frac{(s^1)^+(\rho c_d)^- + (s^1)^-(\rho c_d)^+}{(\rho c_d)^+ + (\rho c_d)^-} + \frac{(\rho c_d)^+(\rho c_d)^-}{(\rho c_d)^+ + (\rho c_d)^-} \llbracket v_1 \rrbracket \tag{15a}$$

$$\check{v}_1 = \frac{\llbracket w^1 \rrbracket}{(\rho c_d)^+ + (\rho c_d)^-} = \frac{\llbracket s^1 \rrbracket}{(\rho c_d)^+ + (\rho c_d)^-} + \frac{(\rho c_d v_1)^- + (\rho c_d v_1)^+}{(\rho c_d)^+ + (\rho c_d)^-}. \tag{15b}$$

The same expanded relations hold for the tangential Riemann values, modulo the substitutions, $1 \rightarrow i$ and $c_d \rightarrow c_s$. That is, for $i = 2, 3$,

$$\check{s}^i = \frac{(w^i)^+(\rho c_s)^- + (w^i)^-(\rho c_s)^+}{(\rho c_s)^+ + (\rho c_s)^-} = \frac{(s^i)^+(\rho c_s)^- + (s^i)^-(\rho c_s)^+}{(\rho c_s)^+ + (\rho c_s)^-} + \frac{(\rho c_s)^+(\rho c_s)^-}{(\rho c_s)^+ + (\rho c_s)^-} \llbracket v_i \rrbracket \tag{16a}$$

$$\check{v}_i = \frac{\llbracket w^i \rrbracket}{(\rho c_s)^+ + (\rho c_s)^-} = \frac{\llbracket s^i \rrbracket}{(\rho c_s)^+ + (\rho c_s)^-} + \frac{(\rho c_s v_i)^- + (\rho c_s v_i)^+}{(\rho c_s)^+ + (\rho c_s)^-}. \tag{16b}$$

The tangential component of the Riemann traction vector is

$$\check{\boldsymbol{\tau}} := \check{s}^2 \mathbf{e}_2 + \check{s}^3 \mathbf{e}_3. \tag{17}$$

The following conditions must be satisfied for the trial contact–stick solution to be accepted as the actual Riemann solution. First, the solution must satisfy the conditions for contact:

$$\bar{s}^1 < 0 \tag{18a}$$

$$\delta = 0 \tag{18b}$$

in which δ is the normal separation across Γ , and \bar{s}^1 is computed according to (16a) even if the contact conditions (18) are violated. In addition, the tractions must not exceed the limits of the chosen constitutive relation for friction. For simplicity, we adopt from here on the isotropic Coulomb friction law. Thus, the tangential traction component of the trial stick solution on Γ must satisfy

$$|\bar{\tau}| \leq k \langle -\bar{s}^1 \rangle_+, \tag{19}$$

in which k is the Coulomb friction coefficient and $\langle \cdot \rangle_+$ is the positive-part (Heaviside) function. If both branches of (18) and inequality (19) are satisfied, we accept the trial contact–stick solution as the Riemann solution for contact and write,

$$(\bar{\mathbf{s}}, \bar{\mathbf{v}}) = (\mathbf{s}, \mathbf{v}). \tag{20}$$

Otherwise, we must investigate the Riemann solutions for separation or the contact–slip case, as described below.

Remark 1. The jump conditions and Riemann solutions for the case where the material interface Γ is perfectly bonded are identical to those for contact–stick except that (14) holds, whether or not the solution satisfies inequalities (18a) and (19). The Riemann solutions presented here apply to bonded, possibly bi-material interfaces between isotropic, linear-elastic materials.

2.2.2. Riemann solution for contact–slip conditions

Contact–slip conditions hold when the trial contact–stick solution satisfies the contact conditions (18), but violates the Coulomb limit (19) such that,

$$|\bar{\tau}| > k \langle -\bar{s}^1 \rangle_+. \tag{21}$$

Inequality (21) is merely one of the indicators for contact–slip response based on the trial contact–stick solution. It does not imply a constraint on the Riemann solution for the slip-mode tractions, $\bar{\mathbf{s}}$; these are governed by the constitutive relation in the friction law and the characteristic structure of the elastodynamic system, as described below.

Fig. 4 depicts the contact–slip Riemann values, $(\bar{\mathbf{s}}, \bar{\mathbf{v}})$, on a material interface for $d = 2$. Again, we define vector and covector components on both sides of the interface with respect to the local coordinate frame on Γ , $\{\xi_j\}$. In contact–slip mode, the tangential velocity may be discontinuous across the contact interface, so kinematic compatibility is only enforced in the normal direction. Thus, (10) holds only for $i = 1$, while the tangential components ($i = 2, 3$) of the velocity field may suffer jumps.

As the point of departure for a new formulation of the dynamic contact–slip Riemann solution, we consider the modifications proposed by Quinn [37] for times when $[[\dot{\mathbf{v}}]] = \mathbf{0}$. Since both (9) and (10) hold for normal components, the normal components of the contact–slip Riemann fluxes for $i = 1$ are identical to their counterparts in the contact–stick solution, cf. (15). The Riemann solutions for the contact–slip traction components are then

$$(\bar{s}^i)^\pm = \begin{cases} \bar{s}^1 & i = 1 \\ ke_v^i \langle -\bar{s}^1 \rangle_+ & [[\dot{\mathbf{v}}]] \neq \mathbf{0}, i = 2, 3 \\ ke_\tau^i \langle -\bar{s}^1 \rangle_+ & [[\dot{\mathbf{v}}]] = \mathbf{0}, i = 2, 3 \end{cases} \tag{22}$$

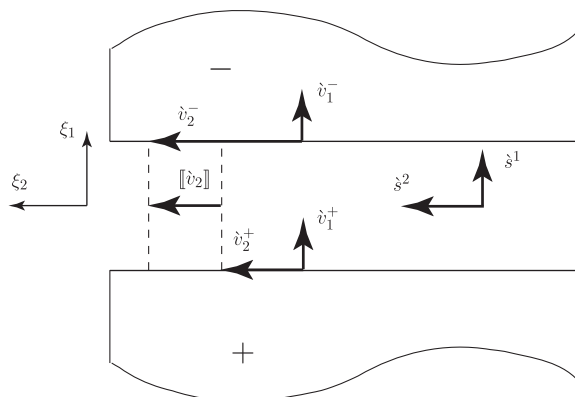


Fig. 4. Traction and velocity components on opposite sides of an interface in contact–slip mode in two spatial dimensions.

in which we reference the unit vectors, $\mathbf{e}_v := \mathbf{g}(\mathbb{[\dot{\mathbf{v}}]})/|\mathbf{g}(\mathbb{[\dot{\mathbf{v}}]})|$ and $\mathbf{e}_\tau := \hat{\boldsymbol{\tau}}/|\hat{\boldsymbol{\tau}}|$. We combine (9), (12), and (22) to obtain the Riemann solutions for the contact–slip velocity components:

$$(\dot{v}_i)^\pm = \begin{cases} \tilde{v}_1 & i = 1 \\ (\dot{s}^i/\rho c^i - w^i/\rho c^i)^\pm & i = 2, 3. \end{cases} \tag{23}$$

To the best of our knowledge, the contact–slip Riemann solution comprised of (22) and (23) is an original result. It enforces the same normal velocity on both sides of Γ to ensure that opposing surfaces remain in contact without introducing Lagrange multipliers or other constraint technologies. The tangential Riemann tractions in (22) are consistent with the Coulomb constitutive relation for friction, and they combine with the tangential Riemann velocities in (23) to generate characteristic values that match those of the incoming waves on each side of Γ .

Despite its advantages, the above Riemann solution retains some of the undesirable computational properties of previous formulations. The systems (22) and (23) are coupled and nonlinear, so they must be solved simultaneously with an iterative scheme. The solution is further complicated by issues associated with the dependence of $\hat{\boldsymbol{\tau}}$ on $\mathbb{[\dot{\mathbf{v}}]}$ in the second branch of (22). The function $k\langle -\dot{s}^1 \rangle_+$ is continuous, although not smooth, in \dot{s}^1 . However, the unit vector function, $\mathbf{e}_v(\mathbb{[\dot{\mathbf{v}}]})$ in the second branch of (22) is discontinuous at $\mathbb{[\dot{\mathbf{v}}]} = \mathbf{0}$. Thus, for $\langle -\dot{s}^1 \rangle_+$ an arbitrary, strictly-positive number, $\hat{\boldsymbol{\tau}}$ is discontinuous at transitions from slip to stick modes where $\mathbb{[\dot{\mathbf{v}}]} = \mathbf{0}$. This discontinuous behavior is well documented and requires special numerical treatment as $|\mathbb{[\dot{\mathbf{v}}]}| \rightarrow 0^+$. For example, Quinn [37] reports numerical chatter in the tangential velocity and traction solutions at stick–slip transitions for models based on (22). Karnopp [35] proposes the elimination of slip-mode kinematic degrees of freedom when the magnitude of the relative velocity across a contact interface falls below a specified threshold as one algorithmic remedy. Alternatively, Mostaghel and Davis [36] and Quinn [37] propose regularization of the Coulomb friction law.

To address these problems, we reformulate the Riemann solution for contact–slip to eliminate the traction discontinuity at stick–slip transitions and the strong coupling between the traction and velocity solutions. Specifically, we reformulate (22) to render the tractions $\hat{\boldsymbol{\tau}}$ independent of $\dot{\mathbf{v}}$. This circumvents the above-mentioned numerical issues so that no special algorithmic techniques are needed to negotiate stick–slip transitions. The modified formulation enables improved numerical contact algorithms while still preserving characteristic structure. In contrast to the previous remedies noted above, there is no algorithmic modification of the Coulomb-friction constitutive relation. We only recast the relation to a form that eliminates the problematic discontinuity.

We begin the reformulation by combining (14) and (23) for $i = 2, 3$:

$$\mathbb{[\dot{v}_i]} = \mathbb{[\dot{s}^i/\rho c^i]} - \mathbb{[w^i/\rho c^i]} = (\dot{s}^i - \dot{s}^i)\mathbb{[(\rho c^i)^{-1}]}. \tag{24}$$

Then we substitute \dot{s}^i from (22) into (24) for the case $\mathbb{[\dot{\mathbf{v}}]} \neq \mathbf{0}$ to obtain, for $i = 2, 3$,

$$\mathbb{[\dot{v}_i]} = \left(k \frac{\mathbb{[\dot{v}_i]}}{\mathbb{[\dot{\mathbf{v}}]}} \langle -\dot{s}^1 \rangle_+ - \dot{s}^i \right) \mathbb{[(\rho c^i)^{-1}]} \iff \mathbb{[\dot{\mathbf{v}}]}|\dot{s}^i = \left(|\mathbb{[\dot{\mathbf{v}}]}}| \frac{(\rho c_s)^+(\rho c_s)^-}{(\rho c_s)^+ + (\rho c_s)^-} + k\langle -\dot{s}^1 \rangle_+ \right) \mathbb{[\dot{v}_i]}, \tag{25}$$

in which we have used, $\mathbb{[(\rho c^i)^{-1}]} = -[(\rho c_s)^+ + (\rho c_s)^-]/[(\rho c_s)^+(\rho c_s)^-]$ for $i = 2, 3$. Eq. (25) implies that the tangential components of $\mathbb{[\dot{\mathbf{v}}]}$ agree with $\hat{\boldsymbol{\tau}}$ to within a positive scaling when $\mathbb{[\dot{\mathbf{v}}]} \neq \mathbf{0}$. Thus,

$$\mathbf{e}_v = \mathbf{e}_\tau, \tag{26}$$

when $\mathbb{[\dot{\mathbf{v}}]} \neq \mathbf{0}$.² Combining (14), (22), (23), (25), and (26), we obtain the reformulated contact–slip Riemann solution,

$$\dot{s}^i = \begin{cases} \dot{s}^1 & i = 1 \\ ke_\tau^i \langle -\dot{s}^1 \rangle_+ & i = 2, 3 \end{cases} \tag{27a}$$

$$(\dot{v}_i)^\pm = \begin{cases} \tilde{v}_1 & i = 1 \\ [v_i + \delta_{ij}(\dot{s}^j - s^j)/\rho c^i]^\pm & i = 2, 3 \end{cases} \tag{27b}$$

in which $(s^j)^\pm = (S^{1j})^\pm|_\Gamma$ where \mathbf{S}^\pm and \mathbf{v}^\pm are as shown in Fig. 3. We only need to compute (27) when both branches of (18) and inequality (21) are satisfied. In that case, the slip solution (27) is the Riemann contact solution, and we write,

$$(\check{\mathbf{s}}, \check{\mathbf{v}}) = (\dot{\mathbf{s}}, \dot{\mathbf{v}}). \tag{28}$$

Eq. (27a) remains valid and continuous, as shown below, even where $\mathbb{[\dot{\mathbf{v}}]} = \mathbf{0}$. Thus, our reformulation circumvents the numerical difficulties associated with (22) as $|\mathbb{[\dot{\mathbf{v}}]}| \rightarrow 0^+$. The normal components of the Riemann solutions for traction and velocity are identical for stick and slip modes, so we only need to check the continuity of the tangential components in (16) and (27).

Consider first the continuity of $\mathbb{[\dot{\mathbf{v}}]}$ under the representation of $\hat{\boldsymbol{\tau}}$ in (27a) at stick–slip transitions. For contact–slip mode, (24), (27a), and $\mathbb{[\dot{v}_1]} = 0$ yield,

² We have proved that (26) holds for friction laws with isotropic constitutive relations, consistent with the present set of caveats. However, He and Curnier [48] show that this equality does not hold for anisotropic friction relations associated with contact interfaces with anisotropic surfaces textures. We discuss possible extensions of our formulation and numerical method to the anisotropic case in 5.

$$\begin{aligned} \llbracket \dot{v}_i \rrbracket &= (|\dot{\tau}| - |\bar{\tau}|)(\mathbf{e}_\tau)^i \llbracket (\rho c^i)^{-1} \rrbracket, \quad i \neq 1 \\ \iff \llbracket \dot{\mathbf{v}} \rrbracket &= \llbracket \dot{\mathbf{v}} \rrbracket = \frac{(c_s \rho)^+ + (c_s \rho)^-}{(c_s \rho)^+ (c_s \rho)^-} (|\dot{\tau}| - |\bar{\tau}|) \mathbf{e}_\tau \end{aligned} \tag{29}$$

Since $|\dot{\tau}| - |\bar{\tau}| = |\dot{\tau}| - k(-\dot{s}^1)_+$, (21) and (29) imply that $\llbracket \dot{\mathbf{v}} \rrbracket > \mathbf{0}$ in slip mode, and $\llbracket \dot{\mathbf{v}} \rrbracket \rightarrow \mathbf{0}$ at transitions from slip to stick mode. In contact–stick mode, (10) and (20) hold, so we always have $\llbracket \dot{\mathbf{v}} \rrbracket = \mathbf{0}$. Therefore, $\llbracket \dot{\mathbf{v}} \rrbracket$ is continuous across stick and slip contact modes under (27a).

Now consider the continuity of $\dot{\tau}$ at stick–slip transitions using (27a) for contact–slip mode. Similar to \mathbf{e}_ν , the unit vector function \mathbf{e}_τ may be discontinuous at $\dot{\tau} = \mathbf{0}$. However, (21) and (29) imply that $|\dot{\tau}| < |\bar{\tau}|$. Thus, $\lim_{|\dot{\tau}| \rightarrow 0} \dot{\tau} = \mathbf{0}$, so that, in contrast to (22), Eq. (27a) provides a continuous representation for $\dot{\tau}$. In fact, (29) implies that $|\dot{\tau}| \rightarrow |\bar{\tau}|$ as $\llbracket \dot{\mathbf{v}} \rrbracket \rightarrow \mathbf{0}$ at slip-to-stick transitions, while (27a) ensures that the directions of $\dot{\tau}$ and $\bar{\tau}$ coincide in slip mode. Therefore, we conclude that $\dot{\tau} = \bar{\tau} \rightarrow \bar{\tau}$ as $\llbracket \dot{\mathbf{v}} \rrbracket \rightarrow \mathbf{0}$ at slip-to-stick transitions. Since (20) holds in stick mode, this guarantees continuity of $\dot{\tau}$ across stick–slip transitions. Thus, the model in (27a) circumvents the problems reported in [37] and requires no special numerical treatments at stick–slip transitions.

Although we prefer (27), Eq. (22) can also be used in existing models that accept the unconstrained traces of the velocity fields on the contact interface in lieu of (23) without resorting to ad hoc algorithmic fixes as in, for example, [35–37]. However, in contrast to the complete reformulation (27), this approach would not enforce the dynamic Riemann solution and, therefore, would not preserve characteristic structure. Nonetheless, it might prove useful in simplifying and improving the robustness of some existing codes.

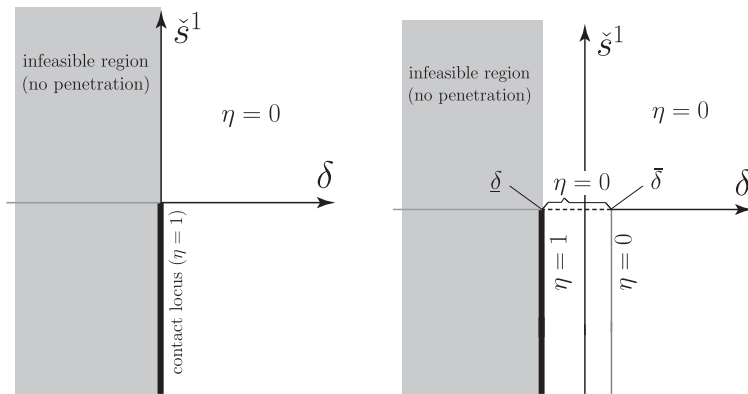
Our formulation of the contact–slip case assumes an isotropic constitutive relation in the friction model. In more general settings, such as the anisotropic friction models investigated by He and Curnier [48], the response at stick–slip transitions might no longer be continuous. Contact models with distinct static and kinetic friction coefficients might also break continuity. Please see the discussion in 5 for further remarks on the applicability of our model and possible extensions to more general contact models.

2.2.3. Riemann solution for separation conditions

Consider possible contact across a perfectly smooth interface, Γ . Contact conditions hold, either for contact–stick or contact–slip, when (18) is satisfied. Fig. 5(a) diagrams the possible combinations of \dot{s}^1 and δ , and shows the contact locus as the negative part of the \dot{s}^1 -axis where both relations in (18) are satisfied. In general, $\dot{\delta} = \llbracket \dot{v}_1 \rrbracket = 0$ in contact mode, since \dot{v}_1 has the same value on both sides of Γ for both the stick and slip cases. The non-penetration constraint for contact implies that $\delta \geq 0$; cf. the infeasible region in Fig. 5(a). Thus, separation conditions hold either when $\dot{s}^1 \geq 0$ and $\delta = 0$, or whenever $\delta > 0$. The parts of Γ where separation conditions hold are treated in the same fashion as prescribed-traction boundaries.

From here on, we assume homogeneous prescribed tractions (traction-free conditions) in separation mode, but non-vanishing prescribed tractions are also possible; e.g., tractions due to viscous fluid loading. The velocity jump conditions (10) are inactive in separation mode; this supports independent velocities on opposing sides of the interface. These conditions generate the separation Riemann solutions, denoted by $(\overset{\circ}{\mathbf{s}}, \overset{\circ}{\mathbf{v}})$:

$$\overset{\circ}{\mathbf{s}} = \mathbf{0}, \tag{30a}$$



(a) Contact scheme without regularization. It is only possible to exit the contact locus at the origin, since contact implies $\dot{\delta} = 0$.

(b) Regularized contact scheme. The separation-to-contact transition region straddles negative part of \dot{s}^1 axis. It is only possible to exit the transition region along its top edge, since $\dot{s}^1 < 0 \Rightarrow \dot{\delta} < 0$.

Fig. 5. Maps of separation ($\eta = 0$) and contact ($\eta = 1$) modes based on the normal separation, δ , and the trial normal contact Riemann traction, \dot{s}^1 , for (a) abrupt and (b) regularized transitions.

$$(\mathring{\mathbf{v}}_i)^\pm = -\left(\frac{W^i}{\rho c^i}\right)^\pm = \left(v_i - \delta_{ij} \frac{s^j}{\rho c^i}\right)^\pm, \quad i = 1, \dots, d. \tag{30b}$$

The Riemann velocity components given by (30b) are generally distinct and independent on opposing sides of Γ .

2.2.4. Contact with a rigid body

Consider a contact system where the material on the $-$ side is much stiffer than the material on the $+$ side. That is, when $r^i := -(\rho c^i)^+ / (\rho c^i)^- \ll 1$ for $i = 1, \dots, d$. The leading negative sign cancels the negative sign of $(c^i)^-$; cf. (11), so r^i is always non-negative. Asymptotic expansions of the Riemann solutions for assumed contact–stick conditions, (14), are given by

$$\mathring{s}^i = (s^i)^+ + (\rho c^i)^+ \llbracket v_i \rrbracket + r^i \{ \llbracket s^i \rrbracket - (\rho c^i)^+ \llbracket v_i \rrbracket \} + \mathcal{O}((r^i)^2) \tag{31a}$$

$$\mathring{v}_i = v_i^- + \delta_{ij} \frac{r^j}{(\rho c^j)^+} \{ \llbracket s^j \rrbracket - (\rho c^j)^+ \llbracket v_j \rrbracket \} + \mathcal{O}((r^j)^2) \tag{31b}$$

for $i = 1, \dots, d$. Taking the limit as $r^i \rightarrow 0$ and using (11), we obtain the Riemann solutions for contact–stick conditions against a rigid body:

$$\mathring{s}^i = \begin{cases} (s^1)^+ + (\rho c_d)^+ \llbracket v_1 \rrbracket, & i = 1 \\ (s^i)^+ + \delta^{ij} (\rho c_s)^+ \llbracket v_j \rrbracket, & i = 2, 3 \end{cases} \tag{32a}$$

$$\mathring{v}_i = v_i^-, \quad i = 1, \dots, d \tag{32b}$$

As expected, only the velocity of the rigid side enters the Riemann solutions. In fact, these solutions coincide with the Dirichlet boundary conditions given in [40,43,47], where the velocity \mathbf{v}^- is prescribed on the boundary of the domain. The Riemann traction solutions involve a traction obtained from the interior trace of the stress field and corrections which ensure preservation of the characteristic structure that depend on the velocity jump. Eq. (27) remains valid for the contact–slip case, provided that the trial contact–stick solutions, $\mathring{\mathbf{s}}$ and $\mathring{\mathbf{v}}$, are obtained from (32). The separation Riemann solutions are still governed by (30), since they do not depend on the characteristics of the rigid side.

2.2.5. Lower spatial dimensions

The Riemann solutions in (14), (27), (30), and (32) are easily specialized for spatial dimensions, $d = 1, 2$. For $d = 2$, there is only one characteristic direction associated with tangential components. Accordingly, (14), (27), (32), (30) are restricted to $i = 2$ for shear modes. The normal and shear wave speeds are the same for plane-strain as for $d = 3$, but we must replace λ with $\hat{\lambda} = 2\mu\lambda / (\lambda + 2\mu)$ for plane-stress conditions. This changes the dilatational wave speed in (7) to $c_d = \sqrt{E / [(1 - \nu^2)\rho]}$, where E and ν are the *elastic modulus* and *Poisson ratio*, respectively. There is no change in the shear wave speed, so only the normal Riemann values for contact–stick and contact–slip are altered in plane-stress models.

For $d = 1$, there is no contact–slip solution. Thus, the Riemann solutions are limited to contact–stick and separation modes, where (15), (30), and (32) with $i = 1$ apply. The longitudinal wave speed in (15) is given by $c_d = \sqrt{E/\rho}$.

2.3. Regularity and regularization of contact–separation transitions

While stick–slip transitions governed by (14) and (27) generate continuous response under the present set of caveats, contact–separation transitions can involve discontinuous response that requires special numerical treatment. In this subsection, we examine separation-to-contact and contact-to-separation transitions and show that only the former generate discontinuous response in the form of weak shocks. These generally require special treatment in numerical implementations, and we propose a regularization for separation-to-contact transitions to complete our scheme for computing Riemann values on spacetime contact manifolds.

2.3.1. Regularity of contact–separation transitions

Fig. 6 depicts the impact of two identical bars that move toward each other with an initial relative velocity, $2V_0$. At the instant of contact, \mathring{s}^1 jumps from 0 to $-\rho c_d V_0$, and $\llbracket v_1 \rrbracket$ jumps from $-V_0$ to 0; cf. (12), (15), (30). That is, the entire velocity jump that exists prior to contact is instantaneously transformed into weak compressive stress shocks that propagate into the two bodies. The weak shocks in this example are entirely due to the abrupt separation-to-contact transition, since there are no discontinuous solution features within the bodies prior to contact.

Now consider a contact-to-separation transition. Initially, we are within the contact locus of Fig. 5(a), where both conditions in (18) are satisfied. It is not possible to move directly from the interior of the contact locus into the separation region by increasing δ from 0 while maintaining a negative value for \mathring{s}^1 , because $\dot{\delta} = 0$ in contact mode; cf. 2.2. The only way to negotiate a contact-to-separation transition is for the trial normal traction, \mathring{s}^1 , to increase from its initial negative value to zero while maintaining $\delta = 0$. If there are no shocks present prior to the transition, the rise in \mathring{s}^1 must be continuous. In fact, (19) and (27a) require that the entire contact traction vector must vanish: $\mathring{\mathbf{s}} = \mathring{\mathbf{s}} \rightarrow \mathbf{0}$ as $\mathring{s}^1 \rightarrow 0^-$. When \mathring{s}^1 reaches 0, the mode switches to separation. Although the trial value, δ , is free to increase from 0, $\mathring{\mathbf{s}} = \mathring{\mathbf{s}} = \mathbf{0}$ must be maintained while separation mode is active; cf. (30a). Thus, continuity of $\mathring{\mathbf{s}}$ is preserved, and contact-to-separation transitions do not generate new shocks.

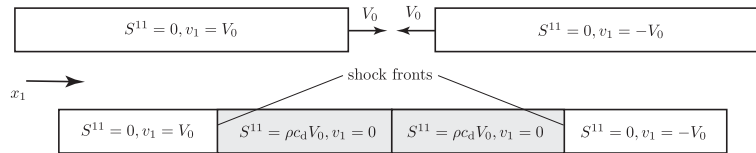


Fig. 6. Axial impact of two identical bars: separation-to-contact transition generates weak shocks in stress and velocity fields. Top: prior to contact; bottom: shock fronts propagate to left and right of contact interface after contact.

In summary, abrupt transitions from separation to contact typically generate weak shocks. On the other hand, contact-to-separation transitions and transitions in either direction between contact–stick and contact–slip modes generate no new shocks under the caveats of our model and the modified contact–slip formulation (27). Accordingly, only separation-to-contact transitions require special treatment in computation. This represents a significant simplification of the algorithmic requirements relative to previous numerical contact models.

2.3.2. Regularization of transitions from separation to contact

We propose a regularization scheme that enhances convergence and controls Gibbs-type artifacts due to weak shocks generated by separation-to-contact transitions. Rather than treat these as abrupt events, the regularization scheme diagrammed in Fig. 5(b) describes a gradual transition that begins when the separation, δ , reduces below the upper regularization limit, $\bar{\delta}$, and ends when δ further reduces to a lower limit, $\underline{\delta}$. The regularization parameters include $(\bar{\delta}, \underline{\delta}) \in \mathbb{R}^2 : \underline{\delta} \leq 0 \leq \bar{\delta}, \bar{\delta} - \underline{\delta} = \epsilon \kappa_u$ in which $\kappa_u > 0$ is a characteristic length scale associated with the displacement solution and $0 < \epsilon \ll 1$. It is convenient to introduce the nondimensional separation, $\delta' := (\bar{\delta} - \delta) / (\bar{\delta} - \underline{\delta})$. For purposes of temporal analysis in our construction of regularization functions below, it is useful to introduce the times \underline{t} and \bar{t} at the start and end of the transition at a given location on the contact interface; i.e., the times when $\delta = \bar{\delta}$ and $\delta = \underline{\delta}$, and the nondimensional time, $t' := (t - \underline{t}) / (\bar{t} - \underline{t})$, such that nondimensional separation, δ' , decreases as nondimensional time, t' , increases. These additional temporal parameters are for analysis purposes only; they are not needed in numerical computations where they would be difficult to identify.

The non-negative value, $-\underline{\delta}$, represents the interpenetration when the regularized transition to contact is complete. One of the goals driving the design of our regularization scheme is to ensure that the interpenetration never exceeds this value while maintaining a well-conditioned system. Many existing contact algorithms use penalty methods to enforce constraints against interpenetration [8–12]. In these schemes, the maximum interpenetration grows with the magnitude of the compressive normal contact traction, so these methods do not enforce a bound on interpenetration. Although large penalty values may be used to reduce interpenetration, this can generate ill-conditioned, stiff systems that might even render the numerical method unstable. In contrast, the regularization proposed below enforces $\delta \geq \underline{\delta}$ by construction without degrading the system’s conditioning. We arbitrarily choose $\bar{\delta} = 0$ and $\underline{\delta} < 0$ in the numerical examples reported in 4. Other choices might be equally valid. For example, interpenetration would be entirely precluded if we select $\underline{\delta} = 0$ and $\bar{\delta} > 0$.

We introduce an interpolation variable, $\eta \in [0, 1]$, such that $\eta = 1$ signifies pure contact response, and $\eta = 0$ indicates pure separation response. We then use η to interpolate between the Riemann solutions for pure contact and pure separation,

$$\mathbf{s}^* = \eta \check{\mathbf{s}} + (1 - \eta) \overset{\circ}{\mathbf{s}} = \eta \check{\mathbf{s}} \tag{33a}$$

$$\mathbf{v}^* = \eta \check{\mathbf{v}} + (1 - \eta) \overset{\circ}{\mathbf{v}}, \tag{33b}$$

in which $\check{\mathbf{s}}$ and $\check{\mathbf{v}}$ are contact Riemann solutions, given for either contact–stick or contact–slip conditions by (15) or (27), while $\overset{\circ}{\mathbf{s}} = \mathbf{0}$ and $\overset{\circ}{\mathbf{v}}$ are separation Riemann solutions given by (30).

Combining relations (15a) and (30b), we obtain

$$\llbracket \overset{\circ}{\mathbf{v}}_1 \rrbracket = \frac{(\rho c_d)^+ + (\rho c_d)^-}{(\rho c_d)^+ (\rho c_d)^-} \check{s}^1. \tag{34}$$

This simple relation between the separation-mode and contact-mode responses reflects the fact that the normal component of any characteristic impinging on Γ is transformed entirely into either a velocity jump or a traction in the respective modes. Since $\llbracket \check{\mathbf{v}}_1 \rrbracket = 0$, and in view of (34), we obtain the following result for the regularized rate of separation during separation-to-contact transitions:

$$\dot{\delta} = \llbracket \dot{\mathbf{v}}_1 \rrbracket = (1 - \eta) \llbracket \overset{\circ}{\mathbf{v}}_1 \rrbracket = (1 - \eta) \frac{(\rho c_d)^+ + (\rho c_d)^-}{(\rho c_d)^+ (\rho c_d)^-} \check{s}^1. \tag{35}$$

The regularized rate of separation vanishes when full contact is achieved at $\eta = 1$, so that $\delta \geq \underline{\delta}$ is implicitly enforced. Eq. (35) also indicates that $\check{s}^1 < 0 \Rightarrow \dot{\delta} < 0$. Thus, while it is possible to enter, it is not possible to exit the transition region in Fig. 5(b) along its right edge. The only exit possible is along the top edge where η changes discontinuously. This structure is consistent with our intent that the regularization should only apply to separation-to-contact transitions, with no regularization in the reverse direction.

We next express η as a function of the nondimensional separation, δ' , and \bar{s}^1 to facilitate construction of regularization models. Overall, we model η with three branches, corresponding to pure separation, the regularized transition, and pure contact,

$$\eta = \begin{cases} 0 & : \delta' < 0 \text{ or } \bar{s}^1 \geq 0 \\ f(\delta') & : 0 \leq \delta' \leq 1 \text{ and } \bar{s}^1 < 0, \\ 1 & : \delta' > 1 \text{ and } \bar{s}^1 < 0 \end{cases} \tag{36}$$

in which the function, $f : [0, 1] \rightarrow [0, 1]$, determines the response in the regularization region that straddles the negative part of the \bar{s}^1 axis. Fig. 5(b) diagrams the overall regularization scheme for separation-to-contact transitions.

The following requirements govern the choice of f :

1. $f(0) = 0$ and $f(1) = 1$ so that the regularization is at least C^0 for $\bar{s}^1 < 0$.
2. f is smooth and monotone-increasing.
3. The separation-to-contact transition, as determined by f and the evolution of δ' , is well distributed over the transition time interval. In other words, $d\eta/dt' > 0$ is bounded above by a value that is reasonably close to unity.

The third requirement prevents overly rapid transitions that can generate numerical artifacts and undermine the stability of the underlying numerical method, thereby defeating the intended regularization. It is useful to introduce a temporal representation for normal separation to investigate this requirement, $\delta' = h(t')$, in which $h : [0, 1] \rightarrow [0, 1]$ is monotone increasing. Then $\eta = g(t')$ where $g := f \circ h \iff f = g \circ h^{-1}$.

Next we derive a useful approximation for the function h corresponding to a given choice of the function g . Since the duration of regularized separation-to-contact transitions should be very short, it is reasonable to approximate $\bar{s}^1 < 0$ with a constant value during these intervals.³ Thus, we write $\bar{s}^1 \approx -\sigma_0$ during the transition, in which $\sigma_0 > 0$ is a constant. Integration of Eq. (35) then yields:

$$h(t') \approx \frac{(\rho c_d)^+ + (\rho c_d)^-}{(\rho c_d)^+ (\rho c_d)^-} \left(\frac{\bar{t} - t'}{\bar{\delta} - \underline{\delta}} \right) \sigma_0 \int_0^{t'} [1 - g(\tau)] d\tau \tag{37}$$

Since $h(t') = t' = 1$ at the end of a transition, (37) implies

$$\bar{t} - t' \approx \frac{(\rho c_d)^+ (\rho c_d)^-}{(\rho c_d)^+ + (\rho c_d)^-} \left(\frac{\bar{\delta} - \underline{\delta}}{\sigma_0 \int_0^1 [1 - g(\tau)] d\tau} \right). \tag{38}$$

Thus, (37) simplifies to

$$h(t') \approx \frac{\int_0^{t'} [1 - g(\tau)] d\tau}{\int_0^1 [1 - g(\tau)] d\tau}. \tag{39}$$

Recalling $f = g \circ h^{-1}$, we use the inverse of h in (39) and the specified function g to approximate f .

For purposes of computation, it is generally more convenient to use the representation, $\eta = f(\delta')$, because δ' can be evaluated directly from the current displacement fields. Moreover, the parameter $\underline{\delta}$ in the definition of δ' provides direct control of the maximum permissible interpenetration in this representation, a feature with some physical appeal (see above discussion vs. penalty methods). The alternative representation, $\eta = g(t')$, is problematic because the computation of t' requires keeping track of t' for each point on the contact interface. Although, we prefer to compute with the f representation, it is still important to derive f from a well-behaved function g to ensure satisfaction of the third requirement.

The following additional properties are desirable for g , although they are difficult to realize simultaneously.

- A An explicit approximation for h^{-1} based on (39) is available so that a convenient explicit approximation for f is available for computation.
- B Substituting g for f and t' for δ' in (36) yields $\eta \in C^1(\Gamma)$ for $\bar{s}^1 < 0$. This improves the regularity of the solution we approximate with SDG basis functions on Γ , resulting in better convergence rates and milder numerical artifacts at separation-to-contact transitions.

Table 1 presents a few example choices for g that satisfy requirement 3 and the corresponding functions, h, h^{-1} , and f . The selections for g in the first two rows also satisfy Property A, but not Property B, since we only obtain $\eta \in C^0(\Gamma)$ for $\bar{s}^1 < 0$. The example in the third row satisfies Property B, but not Property A. In such cases, given δ' , we compute η by first solving numerically for t' at each point on Γ using the nonlinear equation, $\delta' = h(t')$, and then substituting the result into g . We use this approach and the model in the third row of Table 1 for all the numerical examples in 4. Since the spacetime elements that involve separation-to-contact transitions represent a small fraction of the total, the impact of computing the regularization

³ This assumption does not imply that the Riemann values for stress and velocity are constant during the transition. Even if the strength of the impinging characteristic is constant, the form of the Riemann solution must still evolve from a negative relative velocity with zero contact traction at the start of the transition to a contact traction having a negative normal component with zero relative velocity at the end; cf. (33).

Table 1

Selected regularization functions, g , and corresponding functions h, h^{-1} , and f based on (39). Entries ‘–’ indicate no explicit form available. Selections for g in first two rows imply $\eta \in C^0(\Gamma)$ for $\bar{s}^1 < 0$; in third row, $\eta \in C^1(\Gamma)$ for $\bar{s}^1 < 0$.

$g(t')$	$h(t')$; cf. (39)	$h^{-1}(\delta')$	$f(\delta') = g \circ h^{-1}$
t'	$2t' - (t')^2$	$1 - \sqrt{1 - \delta'}$	$1 - \sqrt{1 - \delta'}$
$1 - \cos(\frac{\pi}{2}t')$	$\sin(\frac{\pi}{2}t')$	$2/(\pi \sin^{-1} \delta')$	$1 - \sqrt{1 - (\delta')^2}$
$\frac{1 - \cos(\pi t')}{2}$	$t' + \frac{1}{\pi} \sin(\pi t')$	–	–

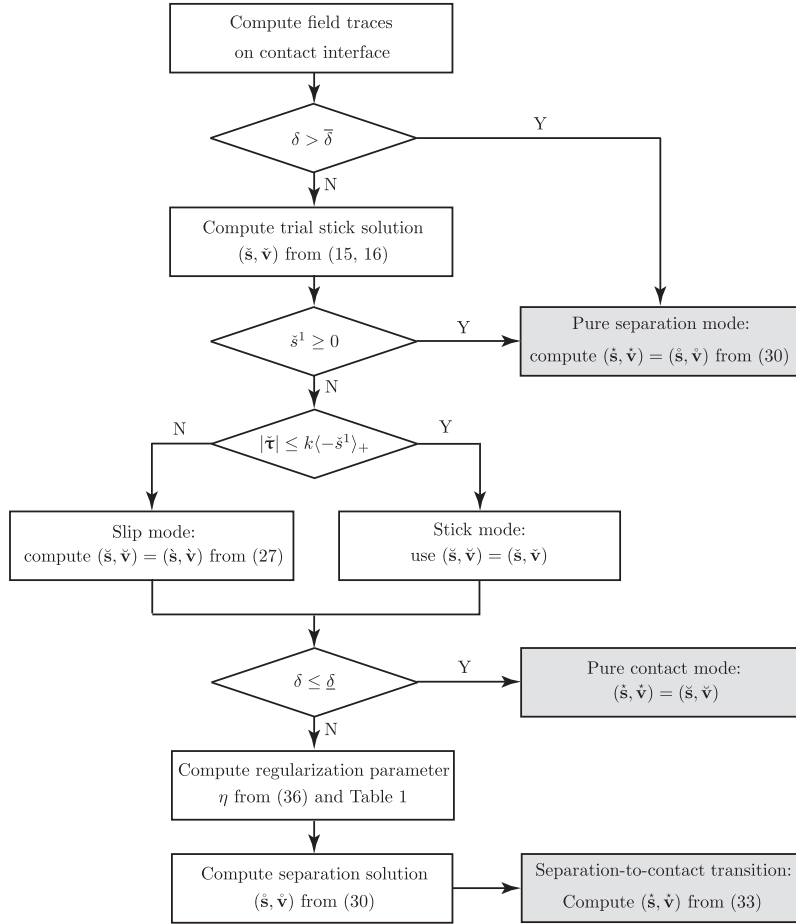


Fig. 7. Flowchart for identification of the contact mode and computation of the regularized Riemann solution. The gray boxes to the right display three possible outcomes.

on the overall solution cost is small in the discontinuous Galerkin implementation described in 3. We have also obtained acceptable results with the simpler models in the first two rows of Table 1.

This continuum level regularization can be incorporated into various numerical schemes. We briefly discuss how the time step in a time marching method may be modified due to contact regularization. Eqs. (35), (38), and the definition of σ_0 imply,

$$\bar{t} - \underline{t} \approx \frac{1}{\int_0^1 [1 - g(\tau)] d\tau} \frac{\bar{\delta} - \underline{\delta}}{[\mathbf{v}_1^*]}. \tag{40}$$

While $\int_0^1 [1 - g(\tau)] d\tau$ and $\bar{\delta} - \underline{\delta}$ are constants of the regularization, the dependence on the jump in separation Riemann velocities, $[\mathbf{v}_1^*]$, implies that the faster two points go into contact, the shorter the regularization time.⁴ In a time discretization method, the time step size and integration scheme may be influenced by the separation-to-contact transition times for points in imminent contact, depending on the details of the given method.

⁴ The term $[\mathbf{v}_1^*]$ incorporates a traction-based correction to the interior velocity jumps that ensures preservation of characteristic values; cf. (30b).

The flowchart in Fig. 7 diagrams the algorithm for identifying the active contact mode and computing the regularized Riemann solutions for traction and velocity, $\begin{pmatrix} \mathbf{s}^* \\ \mathbf{v}^* \end{pmatrix}$, at any point on Γ . In practice, this is typically applied independently at individual quadrature points on Γ .

3. Implementation of the dynamic contact model within a spacetime discontinuous Galerkin method

Although the proposed contact model can be implemented with a variety of numerical models for dynamic response, we describe here a specific implementation within the *spacetime discontinuous Galerkin* (SDG) finite element model for linearized elastodynamics [40,44,43], the model we used to generate the numerical results presented in 4. It is distinct from most other SDG methods in that the solution process generates fully unstructured spacetime grids that satisfy a special *causality constraint*. This enables an advancing-front procedure that interleaves incremental spacetime meshing with local finite element solutions on small clusters of spacetime elements. The resulting asynchronous solution scheme avoids the artificial coupling that limits the performance of conventional time-marching methods and offers several desirable features: element-wise conservation, preservation of characteristic structure across element boundaries, continuous adaptive meshing without error-prone projections, and linear computational complexity in the number of spacetime elements.

We briefly review the SDG algorithm and formulation and describe extensions that incorporate the proposed Riemann solutions for dynamic contact. A detailed description of the SDG model is not required for this purpose and is outside the scope of this paper. The interested reader should consult previous publications cited here for a more complete development.

3.1. Causality-based spacetime meshing and solution scheme

Our SDG solver works with unstructured spacetime meshes, such as the simple example in $1d \times \text{time}$ in the top part of Fig. 8. The inclined arrows indicate the characteristic directions (wave trajectories). In this example, waves travel to the right and left from each point at equal, finite speeds. Our SDG solution scheme imposes a *causality constraint* on the mesh geometry that requires each element facet to be faster (*i.e.*, closer to horizontal) than the fastest wave speed. Thus, all element facets are *space-like* in the terminology of relativity theory, and information flows in only one direction across each element facet. Accordingly, the later facets of a given element are purely outflow surfaces, and the earlier facets are purely inflow. This structure ensures that the solutions in the two shaded elements depend only on the solutions in the earlier elements adjacent to their inflow facets. The solutions in these earlier elements, however, do not depend on the solutions in the shaded elements.

This asymmetric dependency between solutions in adjacent elements generates a partial element ordering by which the global solution can be computed locally, one element at a time. For example, consider the four level-1 elements along the initial-time boundary. The solution in each of these depends only on the initial data along each element’s bottom facet and, in the case of the leftmost and rightmost elements, on prescribed boundary data. The level-1 element solutions can be computed locally and in parallel if multiple computational cores are available. Any level-2 element can be solved as soon as its immediate level-1 neighbors have been solved, even if other level-1 elements remain unsolved. Thus, causal SDG meshes enable asynchronous, element-by-element solutions with linear complexity.

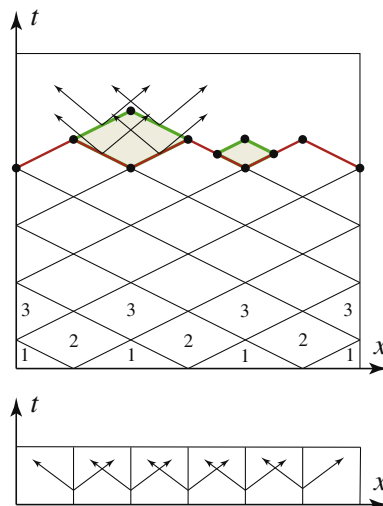


Fig. 8. SDG Solution scheme on causal spacetime mesh (top). Global coupling in noncausal mesh (bottom).

The structured mesh at the bottom of Fig. 8 corresponds to a single step in a conventional time-marching scheme. The characteristic directions indicate symmetric coupling between solutions in adjacent elements. This dependency spreads globally, so that all elements must be solved simultaneously. This undesirable global coupling is entirely an artifact of the traditional noncausal discretization; it does not reflect the true structure of the underlying PDE.

In practice, we replace the individual elements in Fig. 8 with small clusters of simplex elements called *patches*, where only the exterior patch facets are subject to the causality constraint. For example, in $2d \times$ time, a cluster of tetrahedral spacetime elements comprises each patch, as in Fig. 9. We implement an advancing-front meshing/solution procedure. In each step, the *Tent Pitcher* algorithm [45,46,42] advances in time a vertex in the space-like *front mesh* to define a local front update; the causality constraint limits the maximum time increment at the vertex. A small mesh of spacetime simplices covers the region between the old and new fronts to form a new patch. We immediately solve each new patch as a local finite element problem, store the solution, and then locally update the current front mesh to the patch's outflow facets. We repeat this patch-by-patch meshing/solution procedure at front vertices that are local minima in time until the entire spacetime analysis domain is solved.

3.2. Adaptive spacetime meshing

The local spacetime structure of the SDG solver enables a powerful approach to dynamic adaptive meshing. An error indicator is computed for each new patch solution. If the error is acceptable, the patch solution is accepted and stored for use as inflow data for subsequent patches. If the error is too large, the patch is rejected and the solver passes a demand for mesh refinement to the meshing code. If the error is too small, the patch is accepted and a request for subsequent mesh coarsening is issued. Adaptive Tent Pitcher responds to refinement demands by refining the front mesh before restarting the patch-generation procedure. This generates corresponding refinement in the spacetime mesh. For example, the smaller shaded element in Fig. 8 is the result of bisection refinements applied to two segments of the old front mesh.

In $2d \times$ time, we implement common adaptive meshing operations, such as vertex-deletion, edge flips, and vertex motion, as special spacetime patches, Fig. 10. This contrasts with the instantaneous mesh modifications applied between time steps in conventional adaptive meshing algorithms that require expensive and error-prone projections of the solution from the old mesh onto the new mesh. Since the special SDG patches conform to both the old front mesh on their inflow facets and to the new front mesh on their outflow facets, no solution projection is needed, and high-order accuracy is preserved.

We can achieve strong, dynamic refinement because the adaptive meshing and the patch solutions are local operations that share the same granularity within the SDG algorithm. This contrasts with conventional adaptive methods, where remeshing is typically a global operation that is only applied after several time steps have been computed. As seen in Fig. 11, SDG adaptive meshing closely tracks dynamic solution features, such as the trajectories of multiple wavefronts in a crack-tip wave scattering model. In the present contact application, mesh refinement is localized in space and time to resolve sharp transitions between contact modes without triggering global patterns of mesh refinement or reductions in time-step size.

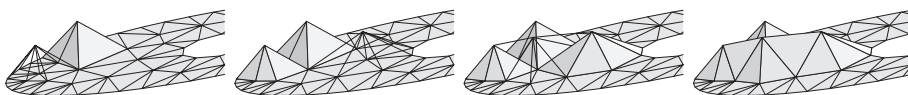


Fig. 9. Pitching patches in $2d \times$ time; the time-axis is vertical. The local causality constraint limits patch duration. Wireframe renderings depict new patches of tetrahedra that are ready to be solved. Opaque surfaces reflect local updates to the current front mesh after a new patch has been solved (reproduced from [40]).

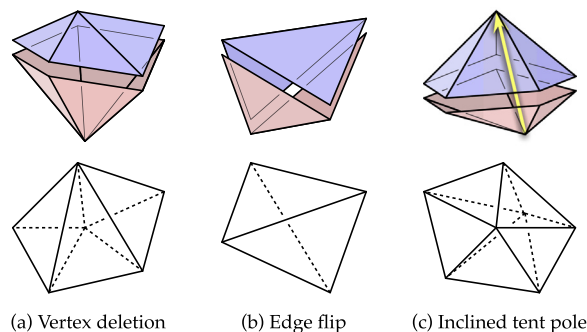


Fig. 10. Adaptive meshing operations via special spacetime patches (top) vs. conventional $2d$ remeshing operations (bottom). Inclined tent poles (c) describe vertex motion, as in moving-mesh models, for tracking discrete solution features or continuous mesh smoothing (reproduced from [49]).

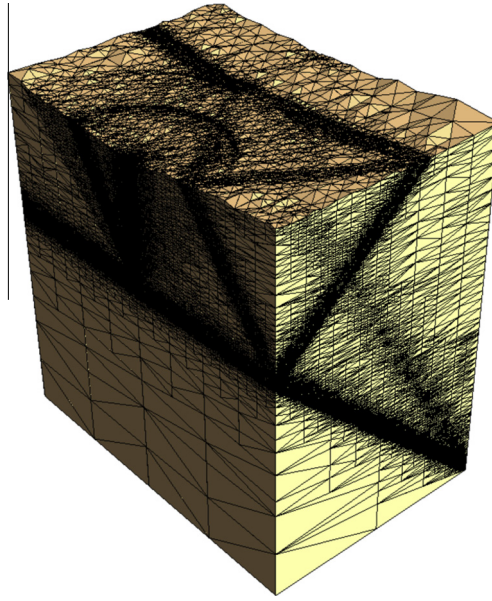


Fig. 11. Adaptive spacetime mesh for an elastodynamic simulation of crack-tip wave scattering in $2d \times \text{time}$ (reproduced from [42]). The vertical direction represents time.

3.3. Spacetime formulation of elastodynamics

We summarize here a discontinuous Galerkin formulation of linear elastodynamics localized to a spacetime subdomain with a suitably regular boundary across which the solution fields may suffer jumps. We associate these subdomains with individual spacetime elements in our SDG discretization. Our formulation follows the development in [40,44,43] which is based on differential forms notation and the exterior calculus on manifolds. This approach, although it might be unfamiliar to some readers, is particularly well-suited to spacetime mechanics formulations. It provides a direct, coordinate-free notation that can be used to express fluxes across interfaces with arbitrary orientations in spacetime and circumvents problems relating to frame invariance that arise with traditional tensor notation. For example, invariant definitions for inner product, vector magnitude, and normal vectors on a d -manifold with arbitrary orientation are not available in the spacetime setting for classical mechanics. A complete development of the forms notation, as presented in the above-cited publications, is rather technical. Fortunately, an abbreviated qualitative description of the single-field displacement formulation, cf. [40,44], is sufficient to explain the incorporation of the Riemann solutions for dynamic contact into the SDG model.

Balance of linear momentum is only weakly enforced in the one-field model, and we focus on this relation first. Given any spacetime domain \mathcal{Q} with a suitably regular boundary, momentum balance is written in forms notation as

$$\int_{\partial\mathcal{Q}} \mathbf{M} = \int_{\mathcal{Q}} \rho \mathbf{b} \tag{41}$$

in which \mathbf{M} is the spacetime d -form that delivers the flux of linear momentum across any spacetime d -manifold, ρ is mass density, and \mathbf{b} is the $(d + 1)$ -form for body force per unit mass. We denote differential forms in italic bold fonts and use upright bold fonts for their vector and tensor coefficients. For example, \mathbf{S} and \mathbf{S} denote, respectively, the differential d -form for stress and the stress tensor field. The form \mathbf{M} must account for both the spatial and temporal components of the momentum flux to address d -manifolds with arbitrary spacetime orientation. Specifically, the stress, \mathbf{S} , and the d -form for linear momentum density, \mathbf{p} , combine to form the spacetime momentum flux: $\mathbf{M} := \mathbf{p} - \mathbf{S}$. This construction in forms notation is the spacetime generalization of the momentum flux delivered by the stress tensor, \mathbf{S} , when it acts on a purely spatial unit normal vector.

We localize the momentum balance Eq. (41) by considering all admissible choices for \mathcal{Q} and applying the Stokes theorem for forms, $\int_{\partial\mathcal{Q}} \mathbf{M} = \int_{\mathcal{Q}} \mathbf{dM}$, in which \mathbf{d} denotes the exterior derivative operator. We obtain

$$\mathbf{dM} - \rho \mathbf{b} = \mathbf{0}. \tag{42}$$

This is the residual statement of the equation of motion written in forms notation.

Kinematic compatibility between displacement and velocity and between velocity and strain are strongly enforced almost everywhere in the one-field model, but only weakly enforced across element boundaries. The linear constitutive relations between strain and stress and between velocity and linear momentum density are also strongly enforced. We combine

the kinematic 1-forms for linearized strain, \mathbf{E} , and velocity, \mathbf{v} , to obtain the spacetime velocity–strain 1-form, $\boldsymbol{\varepsilon} := \mathbf{v} + \mathbf{E}$. The localized form of the velocity–strain compatibility relation is then,

$$\text{sym}(\mathbf{d}\boldsymbol{\varepsilon}) = \mathbf{0}, \tag{43}$$

which establishes the standard relation between the strain rate and the symmetric part of the velocity gradient. Similarly, the local form for displacement–velocity compatibility is

$$\mathbf{i}(\mathbf{d}\mathbf{u} - \boldsymbol{\varepsilon}) = \mathbf{0}, \tag{44}$$

in which \mathbf{u} is the 0-form for displacement, and the temporal insertion operator, \mathbf{i} , extracts the displacement–rate 1-form from $\mathbf{d}\mathbf{u}$ and the velocity 1-form from $\boldsymbol{\varepsilon}$.

Forms coefficients can suffer jumps in our discontinuous Galerkin model, so we must interpret the exterior derivative operator weakly in the sense of distribution theory [50]. Thus, the exterior derivative of a form generally contains a diffuse part and a jump part. Following the convention used in [44], we use $\mathbf{d}\boldsymbol{\alpha}$ to denote the diffuse part of the exterior derivative of any form $\boldsymbol{\alpha}$ and write the jump part separately and explicitly. For example, the jump part of $\mathbf{d}\mathbf{M}$ on the boundary $\partial\mathcal{Q}$ is written as, $\mathbf{M}^* - \mathbf{M}$, in which \mathbf{M}^* is a target value, as determined by a designated Riemann, inflow or prescribed boundary value, and \mathbf{M} is the interior trace of \mathbf{M} on \mathcal{Q} . Similarly, we write the jump parts of $\mathbf{d}\mathbf{u}$ and $\mathbf{d}\boldsymbol{\varepsilon}$ as $\mathbf{u}^* - \mathbf{u}$ and $\boldsymbol{\varepsilon}^* - \boldsymbol{\varepsilon}$. The general expressions for target values on $\partial\mathcal{Q} \setminus \Gamma$ can be found in [40,47]. We describe in 3.4 the interpretation and evaluation of the target values on Γ using the contact Riemann solutions.

We construct a per-element weighted residual statement for our spacetime discontinuous Galerkin finite element model by weakly enforcing both the diffuse and the jump parts of (42) but only the jump parts of (43) and (44) (the diffuse parts of the latter two residuals vanish by construction in the one-field formulation). We denote weighting functions with a superposed \wedge . The primary unknown displacement field, \mathbf{u} , and the corresponding weightings, $\hat{\mathbf{u}}$ on element \mathcal{Q} , lie in the discrete space, $\mathcal{V}_h^{\mathcal{Q}}$, constructed with complete polynomial bases of order k_Q on the interior of spacetime element \mathcal{Q} . Thus, our SDG displacement solutions are continuous within \mathcal{Q} , but allow jumps across $\partial\mathcal{Q}$ relative to solutions in adjacent elements or prescribed initial and boundary data on the boundaries of the spacetime analysis domain. Accordingly, the jump part of the exterior derivative operator is limited to $\partial\mathcal{Q}$. In the one-field formulation, $\boldsymbol{\varepsilon}$ and $\boldsymbol{\varepsilon}^*$ contain the velocity and strain 1-forms on the interior of \mathcal{Q} derived directly from \mathbf{u} and $\hat{\mathbf{u}}$, while \mathbf{M} and \mathbf{M}^* contain the corresponding stress and linear-momentum-density forms as defined by the constitutive relations. We seek $\mathbf{u} \in \mathcal{V}_h^{\mathcal{Q}}$ for all elements \mathcal{Q} , such that

$$\int_{\mathcal{Q}} \mathbf{i}\hat{\boldsymbol{\varepsilon}} \wedge (\mathbf{d}\mathbf{M} - \rho\mathbf{b}) + \int_{\partial\mathcal{Q}} \{\mathbf{i}\hat{\boldsymbol{\varepsilon}} \wedge (\mathbf{M}^* - \mathbf{M}) + (\boldsymbol{\varepsilon}^* - \boldsymbol{\varepsilon}) \wedge \mathbf{i}\hat{\mathbf{M}} + \kappa\hat{\mathbf{u}} \wedge (\hat{\mathbf{u}}_0 - \mathbf{u}_0)\star dt\} = 0 \quad \forall \hat{\mathbf{u}} \in \mathcal{V}_h^{\mathcal{Q}}. \tag{45}$$

The polynomial order k_Q can be adjusted on a per-element basis in an hp -adaptive scheme. The constant κ is introduced to ensure dimensional consistency, and \mathbf{u}_0 denotes the zero-energy part of \mathbf{u} ; cf. [40]. The d -form $\star dt$ is (to within sign) the spatial volume differential and reflects the fact that the characteristics of the displacement–velocity compatibility equation run parallel to the time axis.

The weak form that defines the SDG finite element method for elastodynamics is obtained by applying the Stokes Theorem to the Weighted Residual Statement, (45); cf. [40]. Results of numerical convergence studies are reported in [40,44]. For a sufficiently smooth continuum solution and $k_Q = p$, the L^2 norm of the displacement error over the entire spacetime domain converges at the optimal rate of h^{p+1} . The numerical energy dissipation is provably non-negative, so stability is guaranteed, and it converges as h^{2p-1} .

There are several reasons why we prefer to use Riemann solutions as the target fluxes rather than some other numerical flux, such as a flux average. First, enforcing Riemann fluxes, in comparison to average numerical fluxes, substantially reduces numerical errors when shocks are present [40]. In addition, it is desirable that the element-wise balance properties that are intrinsic to SDG models be defined with respect to the physically correct Riemann fluxes. Riemann fluxes also conform to the principle of causality as it applies to the propagation of characteristic variables in spacetime. The arguments in favor of using Riemann values are particularly strong for linear problems, where Riemann solutions can be easily computed at reasonable cost. We detail the procedure for computing Riemann fluxes on the contact interface in the next subsection.

3.4. Incorporation of the Riemann solutions for dynamic contact

The only modification to the basic SDG formulation (45) needed to implement the proposed contact model involves the proper interpretation of the jump terms and target values on element faces that lie on Γ , i.e., on $\partial\mathcal{Q} \cap \Gamma$. The contact interfaces are material interfaces, so it is easy to show that $\star dt|_{\Gamma} = \mathbf{0}$. Thus, the third jump term in (45) vanishes identically on $\partial\mathcal{Q} \cap \Gamma$, while the momentum flux simplifies to $\mathbf{M}|_{\partial\mathcal{Q} \cap \Gamma} = -\mathbf{S}|_{\partial\mathcal{Q} \cap \Gamma}$. Furthermore, one can show that $(\boldsymbol{\varepsilon} \wedge \mathbf{i}\hat{\mathbf{M}})|_{\partial\mathcal{Q} \cap \Gamma} = (\mathbf{v} \wedge \mathbf{i}\hat{\mathbf{M}})|_{\partial\mathcal{Q} \cap \Gamma}$. Then, after noting that the restriction of the trace of the stress form to $\partial\mathcal{Q}$ delivers the traction form on $\partial\mathcal{Q}$ ($\mathbf{S}|_{\partial\mathcal{Q}} = \mathbf{s}$ on $\partial\mathcal{Q}$), implementation of the contact model only requires setting $\boldsymbol{\varepsilon}^*|_{\partial\mathcal{Q} \cap \Gamma} = \hat{\mathbf{v}}$ and $\mathbf{M}^*|_{\partial\mathcal{Q} \cap \Gamma} = -\hat{\mathbf{s}}$, in which $\hat{\mathbf{v}}$ and $\hat{\mathbf{s}}$ are differential forms for the velocity and traction Riemann solutions on Γ whose tensorial coefficients for

the various contact modes are given in 2.2 and 2.3. Thus, evaluation of $\mathbf{M}^*|_{\partial\mathcal{Q}\cap\Gamma}$ entails proper identification of the active contact mode.

The solutions on individual elements within a patch are coupled through the interior noncausal element faces, including faces intersecting Γ , and the patch-wise solution process is implicit. The contact mode at any point on Γ can change during a patch solution, and the slip-mode friction traction depends on the normal component of the contact traction. This renders (45) nonlinear, so we use Newton–Raphson iterations to solve any patch that is intersected by Γ . This requires a reasonable estimate of the patch solution to initiate the iterations. We construct the initial estimate for \mathbf{u} in each element \mathcal{Q} of the patch by mapping the element’s inflow data for displacement and velocity into a displacement field in $\mathcal{V}_h^{\mathcal{Q}}$ that varies, at most, linearly in time.

At the start of each Newton iteration, we use the current solution estimate to compute the contact mode and the Riemann solution at each quadrature point on $\partial\mathcal{Q}\cap\Gamma$ according to the algorithm diagrammed in Fig. 7. We then use this information to compute a Newton update of the solution estimate. This process repeats until the patch-wise solution converges. We can have distinct contact modes at different quadrature points in the same patch, even for points on the same facet, and the contact mode at an individual quadrature point can change from one iteration to the next. In order to ensure good resolution of regularized separation-to-contact transitions, we limit the range of η within any single element by demanding adaptive refinement when that range exceeds a user-specified tolerance; cf. (33).

The patch-level problem is linear under our assumption of linear elastodynamic response, except in patches that intersect Γ . The patch-by-patch SDG solution scheme naturally exploits this localized nonlinear structure to reduce solution cost since most patches do not require Newton iterations. Therefore, the addition of nonlinear contact causes only a small increase in computational expense over the linear computational complexity of our SDG solution scheme for the linear problem without contact. In this respect, we expect our method to be much more efficient than conventional implicit solvers that do not offer linear complexity in problems without contact and that extend the cost of nonlinear contact iterations to the entire computational domain. Our method’s asynchronous adaptive spacetime meshing further reduces computational cost relative to conventional adaptive procedures where remeshing is performed less frequently and time steps must be kept uniform over either the entire computational domain or, in more advanced adaptive solvers, still sizable subdomains. These efficiencies, specific to our SDG discretization and solver, easily outweigh the cost of the higher dimension of the SDG solution space relative to continuous discretizations.

Overall, our method weakly enforces the jump parts of the compatibility and momentum-balance relations as well as a local matching condition with the Riemann fluxes that preserves the characteristic structure of the regularized system over the entire spacetime domain. This property increases solution accuracy, enhances stability, and to our knowledge, is unique relative to previous numerical models for dynamic contact.

4. Numerical results

This section presents numerical results that demonstrate the SDG implementation of the proposed Riemann solutions for dynamic contact. We begin with a study in one spatial dimension, involving contact between two bars, to investigate the model’s ability to capture contact-mode transitions, especially discontinuous contact–separation transitions. Next, we investigate the model’s ability to simulate frictional contact in a problem involving impact between an elastic body and a rigid surface. Then we present a simulation of a brake pad and disk system to demonstrate the model in a more complex setting where it must capture high-frequency unsteady contact response at high slip velocities.

We use tetrahedral spacetime elements with complete cubic polynomial bases for simulations in $2d \times \text{time}$ in all of the studies reported below. We specialize the two-dimensional material model and boundary conditions to enforce one-dimensional response in the first example. We only present results for C^1 regularizations of the form, $g(t') = 1 - \cos(\pi t')/2$; cf. the third row of Table 1. C^0 models, such as $g(t') = t'$ in the first row of the table, produce similar results, although the solutions are not quite as smooth as those obtained with the C^1 regularization at $\eta = 0, 1$. Although the C^1 model requires a Newton–Raphson procedure to evaluate $f(\delta')$ since an explicit form for h^{-1} is not available, this did not increase significantly the overall cost of the simulation.

4.1. Axial impact between two bars

The problem of axial impact between two bars, although simple to solve analytically, provides a stringent test of a numerical contact model’s ability to capture sharp transitions between contact and separation modes. Fig. 12(a) depicts the geometry and initial conditions for this one-dimensional problem. Two bars, each with length L and unit cross-section area, have an initial gap, $g_0 \geq 0$, and move toward each other with an initial relative velocity, V_0 . The two bars make first contact at time $t_0 = g_0/V_0$. We assume perfectly smooth contact surfaces, so that the separation-to-contact transition is instantaneous and generates a weak shock that propagates into each bar with axial velocity, $c = \sqrt{E/\rho}$, where E is Young’s modulus and ρ is mass density. There might be distinct axial wave velocities when the two bars are comprised of different materials. If the bars are identical, they separate when the axial waves traverse each bar and reflect back to the contact interface at time $t = t_0 + 2L/c$.

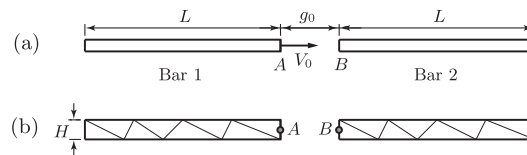


Fig. 12. Axial impact of two bars with equal area. (a) domain description and initial conditions, (b) interpretation in 2d showing spatial discretization in the initial-front mesh. Thickness, to generate unit cross-section area, is not shown. The SDG solver generates a spacetime grid from this initial mesh with strong adaptive refinement that varies in space and time to capture moving wavefronts and contact-mode transitions with high accuracy.

The two-bar axial impact problem is a popular choice for testing numerical methods for dynamic contact, see for example [13,52,53,21,24,54,51,55,25]. Most of these methods use semi-discrete algorithms and rely on special treatments of time integration to limit numerical artifacts at contact-mode transitions. Fig. 13(a) presents results from [51] to illustrate typical examples of these artifacts, including overshoot and oscillations when the bars first come into contact at time t_0 (for this plot only, $g_0 = 0$, so $t_0 = 0$). These oscillations persist throughout the period of contact in some methods, e.g., [25]. We also observe severe oscillations in the velocity field following the contact-to-separation transition at $t = 0.02$. This behavior is observed with almost all the methods cited above. In general, these artifacts cannot be controlled by enriching the spatial and temporal discretizations; other remedies are required. For example, the method described in [13] suppresses these oscillations through a manual modification of the integration parameters at the instant of the contact-to-separation transition. However, this approach might be difficult to automate, and it comes at the cost of increased numerical dissipation.

4.1.1. SDG results using contact Riemann solutions for similar bars

Fig. 12(b) shows the two-dimensional representation of this problem used to test our adaptive SDG contact model. Now the bar is modeled in plane stress with width H and a thickness selected to provide a rectangular cross section with unit area. Fig. 12(b) shows the initial spatial discretization. The Poisson ratio is set to zero to ensure uniaxial response in the 2d model. Accordingly, the results reported below describe only the axial components of the mechanical response. We first solve this problem for $L = 10$, $g_0 = 0.01$, and $V_0 = 0.1$, with Young's modulus $E = 100$ and mass density $\rho = 0.01$. Thus, the axial wave speed is $c = 100$ in both bars which first come into contact at $t_0 = 0.1$. We use $\epsilon = 3 \times 10^{-4}$ and $\kappa_{\mathbf{u}} = L/(cV_0)$ to obtain the regularization parameters for separation-to-contact transitions: $\bar{\delta} = 0$ and $\underline{\delta} = -3 \times 10^{-6}$. The duration of the regularized transition for these parameters is, $\bar{t} - \underline{t} = 2\epsilon L/c = 6 \times 10^{-5}$, a suitably short period relative to the macroscopic time scale of the problem.

We present results from the regularized SDG solution for impact between two identical bars in Fig. 13(b)–(d). The transition from separation to contact starts immediately at t_0 , when $\delta = \bar{\delta}$, and the bars come into complete contact, with $\delta = \underline{\delta}$, at a time that matches well our analytical prediction of the duration of the regularized transition. We observe no spurious oscillations between separation and contact modes; the transition is rapid, smooth and free of undershoot and overshoot. Moreover, there are no numerical artifacts during the period of contact. The bars remain in full contact until reflected waves separate the bars at time $t = 0.3$, consistent with the analytical solution.

Since contact-to-separation transitions do not generate shocks spontaneously, the sharpness of these transitions depend on the sharpness of the incoming tensile wavefronts. In the present example, the tensile wavefronts are reflections of compressive wavefronts originating from the regularized separation-to-contact transition. The tensile fronts carry the same regularized form as the source fronts, so no further regularization is needed at contact-to-separation transitions. In contrast to almost all previous results reported in the literature, there are no post-separation oscillations in the SDG velocity solutions, cf. Fig. 13(b), and only very small overshoots and undershoots in the SDG stress solutions that die out almost immediately, cf. Fig. 13(c). These over/undershoots represent discretization error in the SDG model of sharp wave fronts. However, given the regularized structure of the Riemann solutions in our contact model, these features can be made arbitrarily small with sufficiently tight adaptive tolerances. Axial displacements predicted by the regularized SDG model track the analytical solution very closely; Fig. 13(d).

Sharp spikes are evident in the SDG velocity solutions at $t = 0.5$ in Fig. 13(b). Although these features are not present in the analytical solution for smooth contact surfaces in Fig. 13(a), they do appear in the analytical solution for the regularized contact model. The spikes are due to compressive reflections from the initial regularized separation-to-contact transition that arrive at the contact interface periodically at intervals of 0.4, with a duration of only 6×10^{-5} . These transient events involve transitions into and out of contact during which the contact tractions remain zero. In the exact solution to the regularized model, the contact velocities momentarily attain a common value that coincides with the original contact velocity, $v = 0.05$, before rapidly returning to distinct separation velocities. The analytical solutions for smooth-surface and regularized contact are in close agreement outside of these transient events. Although the SDG solution for the regularized problem does not exactly recover the common contact velocity, the fact that our model captures this exceedingly brief event as well as it does is testament to its precision. Although we do not intend our regularization to model actual micromechanical response, we do expect similar transient features in real physical systems where surface roughness and imperfections result in non-sharp separation-to-contact transitions when observed at sufficiently small time scales.

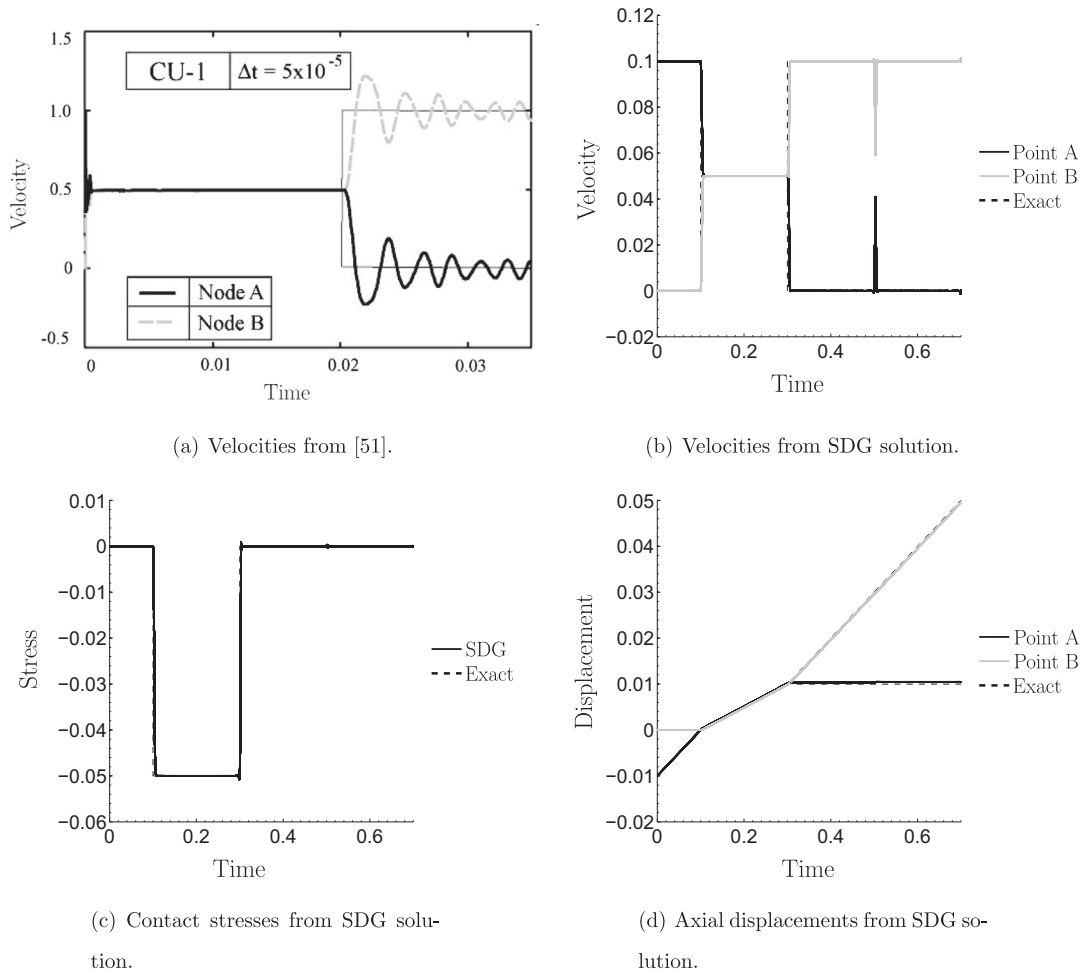


Fig. 13. Axial impact of two identical bars: solution traces from left (A) and right (B) sides of contact interface. The SDG results use regularized Riemann values and adaptive spacetime meshing.

4.1.2. SDG results using contact Riemann solutions for dissimilar bars

Next, we consider axial impact between two bars comprised of dissimilar materials. We retain all of the problem data from the previous example, except we reduce the elastic modulus of bar 1 from 100 to 49 to match an example in [13] (we also use $g_0 = 0.01$, instead of $g_0 = 0$, to highlight the separation-to-contact transition). The results in Fig. 14 are exceptionally accurate. They closely follow the exact solution through sharp contact transitions, are free of numerical oscillations, and only suffer mild undershoots and overshoots.

4.1.3. On the accuracy of the SDG solutions

The accuracy of our solutions is remarkable in comparison to results from previous methods, especially when one considers that they do not rely on any special-purpose procedures beyond the regularization of the Riemann solutions during separation-to-contact transitions. To a large extent, this favorable performance is consistent with, and can be attributed to, properties intrinsic to the h -adaptive SDG method for elastodynamics, as reported in our previous work. In particular, element-wise balance of linear and angular momentum and the preservation of hyperbolic characteristic structure across spacetime element boundaries contribute to the suppression of oscillations and other numerical artifacts. The local balance properties can be attributed to the discontinuous discrete bases, as is typical of discontinuous Galerkin methods. In addition, the scalable patch-wise SDG solution algorithm and unstructured adaptive meshing in space and time provide the precision needed to resolve sharp wavefronts. For example, our solutions start with just 16 triangular elements in the initial front meshes for both the similar and dissimilar bar-impact problems, as shown in Fig. 12. However, the adaptive meshing procedure described in 3.2 generates 1.1 and 0.94 million tetrahedral spacetime elements, respectively, for the two problems. Many more spacetime cells would be required if the algorithm were restricted to maintaining a globally uniform time increment across the domain.

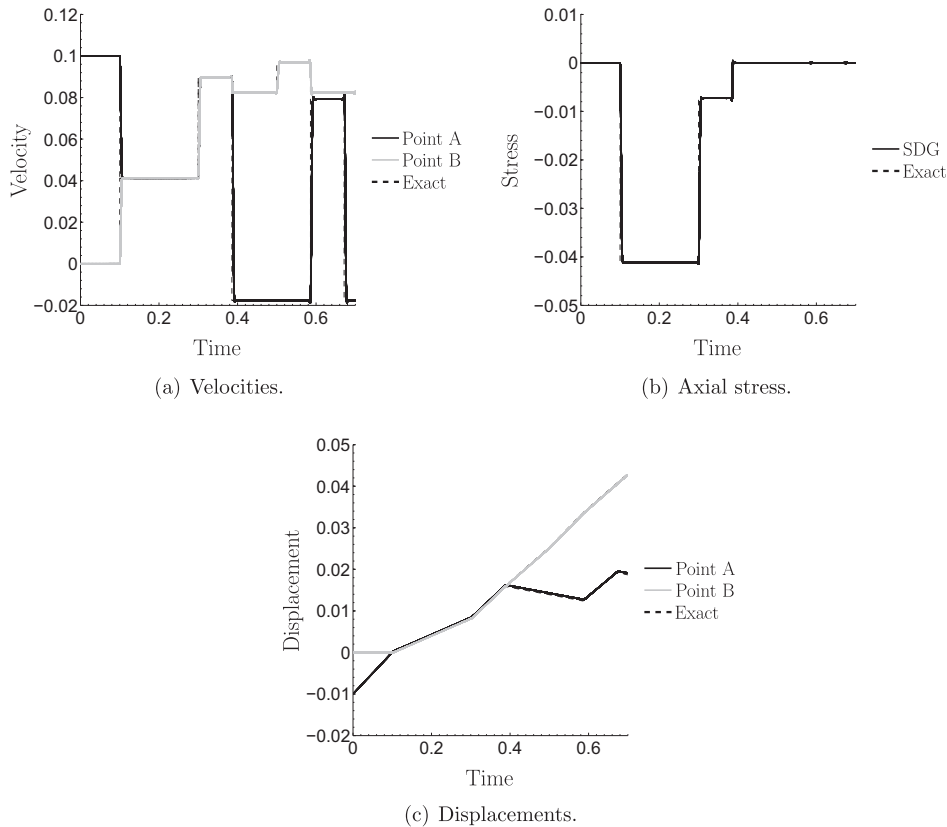


Fig. 14. Axial impact between dissimilar bars: traces on contact interface for SDG model with contact Riemann solutions.

Although the basic SDG algorithm suffers limited but finite over/undershoot at mathematically sharp fronts, these artifacts die out almost immediately after the front passes and they do not pollute the subsequent solution. Unfortunately, the magnitude of these artifacts cannot be controlled at sharp fronts by mesh refinement alone. However, our previous work shows that regularization of sharp fronts reduces over/undershoot and can even eliminate it given sufficient model enrichment. Our regularization of the Riemann contact solutions during separation-to-contact transitions serves the same purpose. The difference, $\bar{\delta} - \underline{\delta}$, provides a length-scale for the regularization, and a sharp front is recovered, in the limit, as this quantity approaches zero. However, the degree of mesh refinement required and the cost of solution increase as the regularization length scale decreases.

The Riemann solutions for the full set of contact modes introduced in this work are essential to the success of our numerical method. Without them, the preservation of characteristic structure at contact interfaces would not be possible, and our model's improved stability characteristics and resistance to oscillations would be reduced. Indeed, the contact Riemann solutions deliver oscillation-free transitions between contact modes, even for coarser adaptive tolerances and relatively large values of the regularization length scale.

4.2. Impact of a square body on a rigid surface

In this example, we examine the frictional contact of a square elastic body following impact against a rigid surface. Fig. 15 depicts the geometry and initial conditions for this two-dimensional problem. The body, with edge length $L = 50$ mm and initial gap $g_0 = 5$ μm , moves toward the rigid surface with initial velocity, $V_0 = 0.5$ m s^{-1} . We model the body with a plain-strain model with Young's modulus $E = 210$ GPa, Poisson ratio $\nu = 0.3$, and mass density $\rho = 7800$ kg m^{-3} . The corresponding dilatational wave speed is $c_d = 6020$ m s^{-1} . The regularization parameters are $\bar{\delta} = 0$ μm and $\underline{\delta} = -0.1$ μm . The initial front mesh consists of 200 triangular elements. However, our adaptive meshing scheme results in a heavily graded mesh in response to contact mode changes and the sharp wave fronts that propagate through the domain after the impact.

Fig. 16 compares histories of the normal separation, δ , and the slip displacement, $\llbracket u_2 \rrbracket$, at point A (cf. Fig. 15) for various values of the friction coefficient: $k = 0, 0.1, 0.2, 0.4$. Fig. 16(a) shows that the regularized separation-to-contact transition starts at $t_0 = g_0/V_0 = 10$ μs , when $\delta = \bar{\delta} = 0$. Full contact is attained when δ reaches $\underline{\delta} = -0.1$ μm which is indistinguishable from zero in the figure. The transition is very sharp, and there are no visible numerical artifacts. The compression wave that

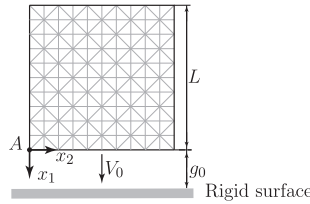


Fig. 15. Square-body impact example: domain description with initial data and front mesh.

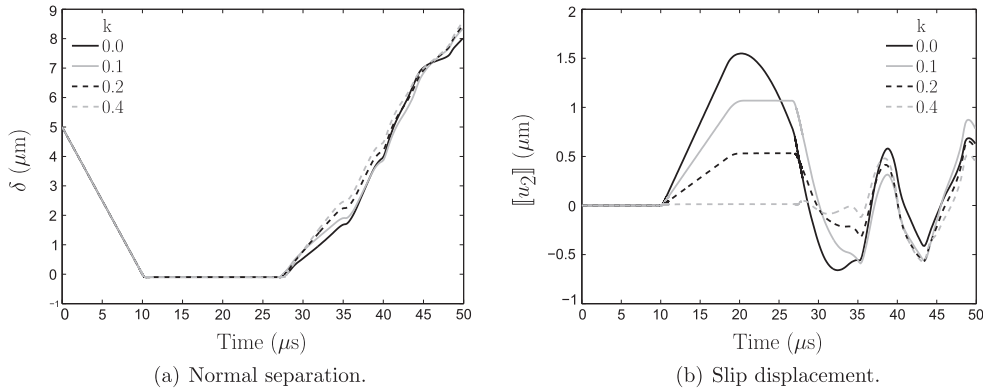


Fig. 16. Square-body impact example: solution at point A.

initiates along the bottom edge of the body at the moment of impact, reflects off the top edge of the body, and returns to the contact interface in the form of a tension wave at $t = t_0 + 2L/c_d \approx 26.6 \mu\text{s}$. The tension wave causes point A to transition back to separation mode. Although the normal separation at A shows little sensitivity to the value of the friction coefficient, we observe slightly larger velocities after the transition to separation for higher values of k .

The slip displacement in Fig. 16(b), on the other hand, is much more sensitive to the value of k . For frictionless contact, where $k = 0$, $[[u_2]]$ peaks at $1.55 \mu\text{m}$ during contact. The peak value drops to $1.07 \mu\text{m}$ and $0.51 \mu\text{m}$ for $k = 0.1$ and 0.2 , as point A eventually sticks to the rigid surface after sliding during the early stages of contact. For the largest value, $k = 0.4$, point A remains in stick mode through almost the entire contact event, with only a small amount of sliding just prior to separation. Nevertheless, we observe tangential oscillations at A, similar to those observed for smaller values of k , after contact is broken.

Fig. 17 shows a time sequence of visualizations for $k = 0.2$ generated by the per-pixel visualization system described in [56]. There are no visible numerical artifacts in Fig. 17(a) in the wake of the compression wavefront generated by the initial impact event. A reflected tension wave arrives at the contact surface at $t = 26.6 \mu\text{s}$ in Fig. 17(c). This initiates transitions to separation at three locations: the center of the contact interface and the two corners, including point A. The three separation zones expand and quickly join up. Contact is soon broken across the entire interface as the elastic body rebounds off the rigid surface, as shown in 17(d).⁵ Overall, a complex wave pattern develops due to interactions between pressure waves, shear waves, and Rayleigh waves propagating along the free edges. Contact mode transitions add further complexity. However, as is evident in these images, the contact mode transitions do not pollute the solution with numerical artifacts beyond a mild softening of wavefronts induced by the separation-to-contact regularization.

4.3. Contact instabilities in a brake-pad model

We investigate the contact instabilities that occur in a model brake system due to a flat, rigid disk sliding under a brake pad [57]. A normal force, F , acts on a rigid plate to press the deformable pad in Fig. 18 against the surface of a second rigid plate that models the disk. Initially, the disk is stationary, and the system is in static equilibrium at time $t = 0$ with zero friction between the pad and the disk. Throughout the simulation, for all times $t > 0$, the disk moves below the pad with a constant sliding speed, \bar{V} , in the direction indicated. We present below numerical results for point A on the contact interface in the local coordinate frame shown in the figure.

⁵ Parallax effects in the perspective rendering of the synthetic height field that depicts the velocity-magnitude as well as strong scaling of the in-plane deformation can affect the apparent gap between the rigid surface and the elastic body in separation mode. This distortion may give a false impression of interpenetration, as seen in Fig. 17(d).

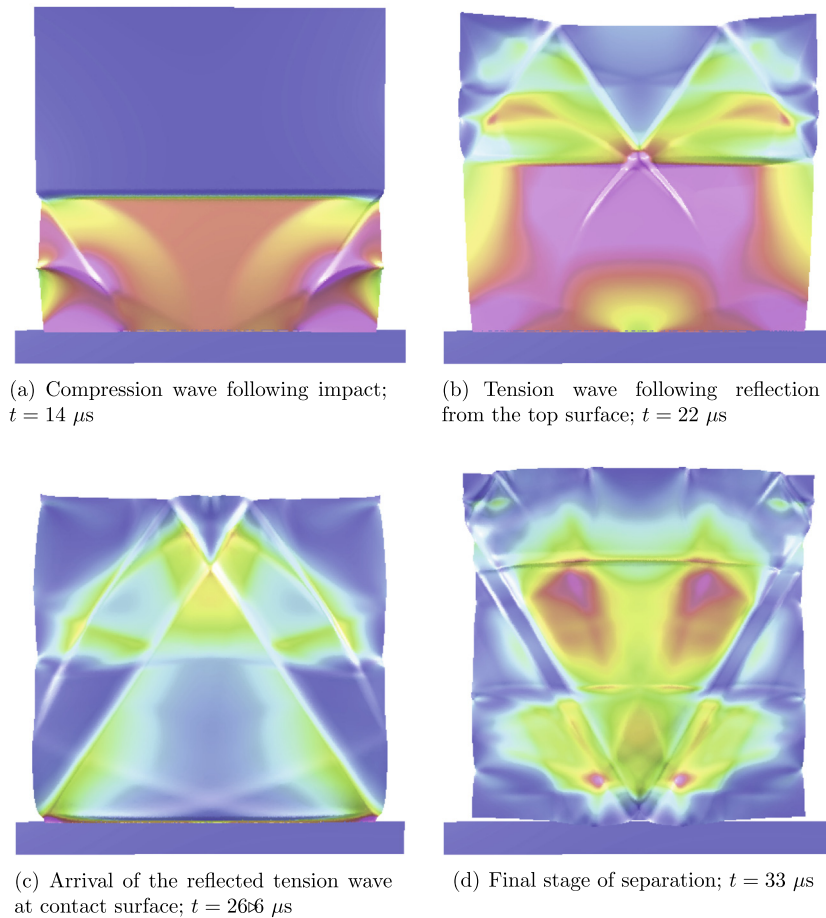


Fig. 17. Visualization of elastic response for square-body impact problem at selected times for $k = 0.2$. In-plane displacements scaled by a factor of 1000. Color depicts strain energy density: blue (low), magenta (high). Magnitude of material velocity is mapped to synthetic height field; resulting surface is light-source shaded and rendered in perspective. (For interpretation of the references to color in this figure legend, the reader is referred to the web version of this article.)

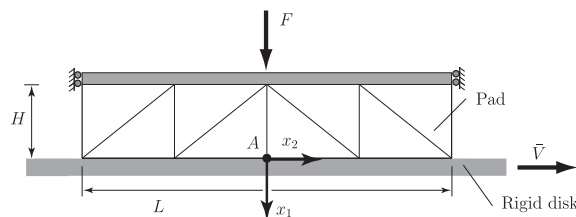


Fig. 18. Brake-pad model: domain description and initial front mesh.

We use the same model parameters given in [57]: $L = 100 \text{ mm}$, $H = 20 \text{ mm}$, and $\bar{V} = 2 \text{ ms}^{-1}$. We use a linear-elastic, plane-strain model for the deformable pad, with Young's modulus $E = 10 \text{ GPa}$, Poisson ratio $\nu = 0.3$, and mass density $\rho = 2000 \text{ kg m}^{-3}$. The corresponding wave speeds are $c_d = 2594 \text{ ms}^{-1}$ and $c_s = 1387 \text{ ms}^{-1}$. The Coulomb friction coefficient is $k = 0.4$, and we use $F = 100 \text{ N}$ to generate the normal contact force resultant per unit thickness. In keeping with the free boundary conditions on the sides of the pad and the zero-friction assumption in the initial configuration, the initial compressive stress, $\sigma_0 = 1 \text{ GPa}$, is uniform over the pad. This generates initial strain components, $E_{11} = -9.1 \times 10^{-5}$ and $E_{22} = 3.9 \times 10^{-5}$, and initial normal displacements along the top surface of the pad, $u = 1.82 \mu\text{m}$. We use the Riemann solutions for contact with a rigid body with regularization parameters, $\bar{\delta} = 0$ and $\bar{\delta} = 18.2 \text{ nm}$, to model dynamic contact for times $t > 0$; cf. 2.2.4 and 2.3.2. The use of the regularized Riemann solutions for dynamic contact is the only difference in our continuum model with respect to the one used in [57].

Sliding motion between contacting bodies can result in an unsteady distribution of contact modes. The contact is called *unstable* when patterns of distinct contact modes form and move along the contact surface as so-called frictional waves. Unstable contact is observed experimentally, investigated theoretically, and modeled numerically in [58–62,57,63]. At low sliding speeds, the instabilities take the form of stick–slip waves, where the tangential tractions that build up in stick mode are suddenly released in the slip phase. As \bar{V} increases to moderate values, the contacting bodies start to separate locally, and stick–slip–separation waves form. Finally, for high slip speeds, the tangential tractions become too large to sustain stick mode, and slip–separation waves dominate.

Fig. 19 shows the development of contact instabilities for a high sliding speed, $\bar{V} = 2 \text{ ms}^{-1}$. In the early stages, $t < 1.5 \cdot 10^{-4} \text{ s}$, point A is almost entirely in slip mode: the normal velocity v_1 is zero, and the tangential velocity v_2 is much smaller than \bar{V} . Also, the normal traction s^1 is nearly uniform and close to the applied static value of $-\sigma_0$. The pad slides back and forth in relatively simple deformations during this early stage. Eventually, separation zones start to form, leading to the development of unstable contact and the propagation of slip–separation waves. This unstable contact behavior results in much higher traction and velocity values. For example, the peak values of s^1 are about 20 times $-\sigma_0$. This increase is due to the reduction of the contact-mode surface area and to dynamic effects from separation-to-contact transitions where the characteristic component from normal velocity transforms rapidly into normal stress. Stick mode, identified by $v_2 = \bar{V}$ and $s^1 < 0$, occurs rarely at this intermediate stage.

Fig. 20 shows a detailed view of the response at point A near the end of the simulation, for $t \in [0.006 \text{ s}, 0.00606 \text{ s}]$. In this figure, stick mode is identified by $u_1 = \bar{\delta} \approx 0, v_1 = 0, v_2 = \bar{V}, s^1 < 0$, and $|s^2| \leq -ks^1$, while slip mode corresponds to $u_1 = \bar{\delta}, v_1 = 0, v_2 \neq \bar{V}, s^1 < 0$, and $s^2 = -ks^1$. Regions where $u_1 < 0, v_1 \neq 0$, and $s^1 = s^2 = 0$ are in separation mode. All solution fields exhibit highly oscillatory behavior with rapid contact mode changes. Fig. 20(d)–(f) show the extent of times where separation, contact–stick, and contact–slip modes are active. In Fig. 20(d), separation mode is fully active when $1 - \eta = 1$. Let $\tilde{\mathcal{I}} := \{t > 0 : |\bar{\tau}| \leq k(-\bar{s}^1)_+\}$ and $\hat{\mathcal{I}} := \{t > 0 : |\bar{\tau}| > k(-\bar{s}^1)_+\}$ be sets of times where stick and slip conditions enter the contact component of the regularization. The plots of $\eta|_{\tilde{\mathcal{I}}}$ and $\eta|_{\hat{\mathcal{I}}}$ in Fig. 20(e) and (f) reveal the times where contact–stick and contact–slip modes are active in the solution. Since \bar{V} is large in this example, stick mode is rare and only holds over very short intervals; cf. Fig. 20(e). For the most part, we observe very rapid transitions between slip and separation modes due to the propagation of slip waves from right to left along the contact surface. The incomplete transitions in Fig. 20(d)–(f) occur when δ does not fully traverse the range, $[\bar{\delta}, \hat{\delta}]$ in our regularized contact model.

Fig. 21 visualizes the brake pad response at selected times to reveal qualitative features of the solution and various stages in the evolution of the pad’s behavior. Fig. 21(a) shows the response at two early times where the pad’s bottom edge deflects laterally in contact–slip mode, and the pad oscillates about a relatively simple mean deformation. The first image shows near-maximum deflection and the second near-minimum deflection within these oscillations. Eventually, contact instabilities arise in the form of slip waves and propagate from right to left along the contact surface. Initially, the slip waves nucleate rarely and aperiodically, but eventually they self-organize to form a quasi-periodic train. Fig. 21(b) shows the onset of this quasi-periodic response, with a train of leftward-propagating slip waves covering the right side of the contact interface. Each slip wave generates a wake wave that propagates into the interior of the pad. A slip wave from the aperiodic response reflects off the free surface at the pad’s lower-left corner to generate a rightward-propagating wave on the contact surface. This and other reflected waves interfere with the leftward waves to disrupt what might otherwise be purer periodic response along the contact surface. At later times, interactions between the reflected waves and the train of slip waves generates very complex wave patterns in the pad, as seen in Figure Fig. 21(c).

Although our solutions are similar to those of [57] in several aspects, including the development of slip–separation instabilities, there are some differences. Our solution predicts larger maximum values for most mechanical fields. For example, our maximum compressive traction and normal and tangential displacement magnitudes are $26\sigma_0, 9 \mu\text{m}$ and $19 \mu\text{m}$,

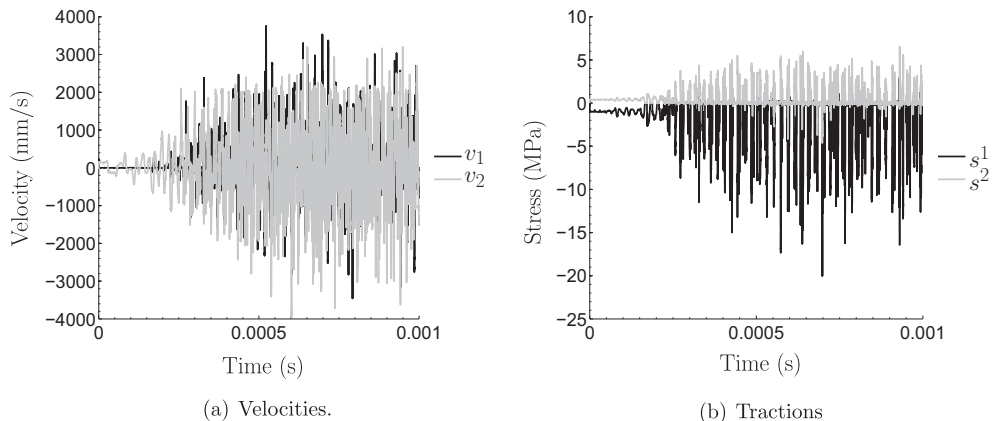


Fig. 19. Brake-pad solution at point A for $t \in [0, 0.001 \text{ s}]$: onset of contact instabilities.

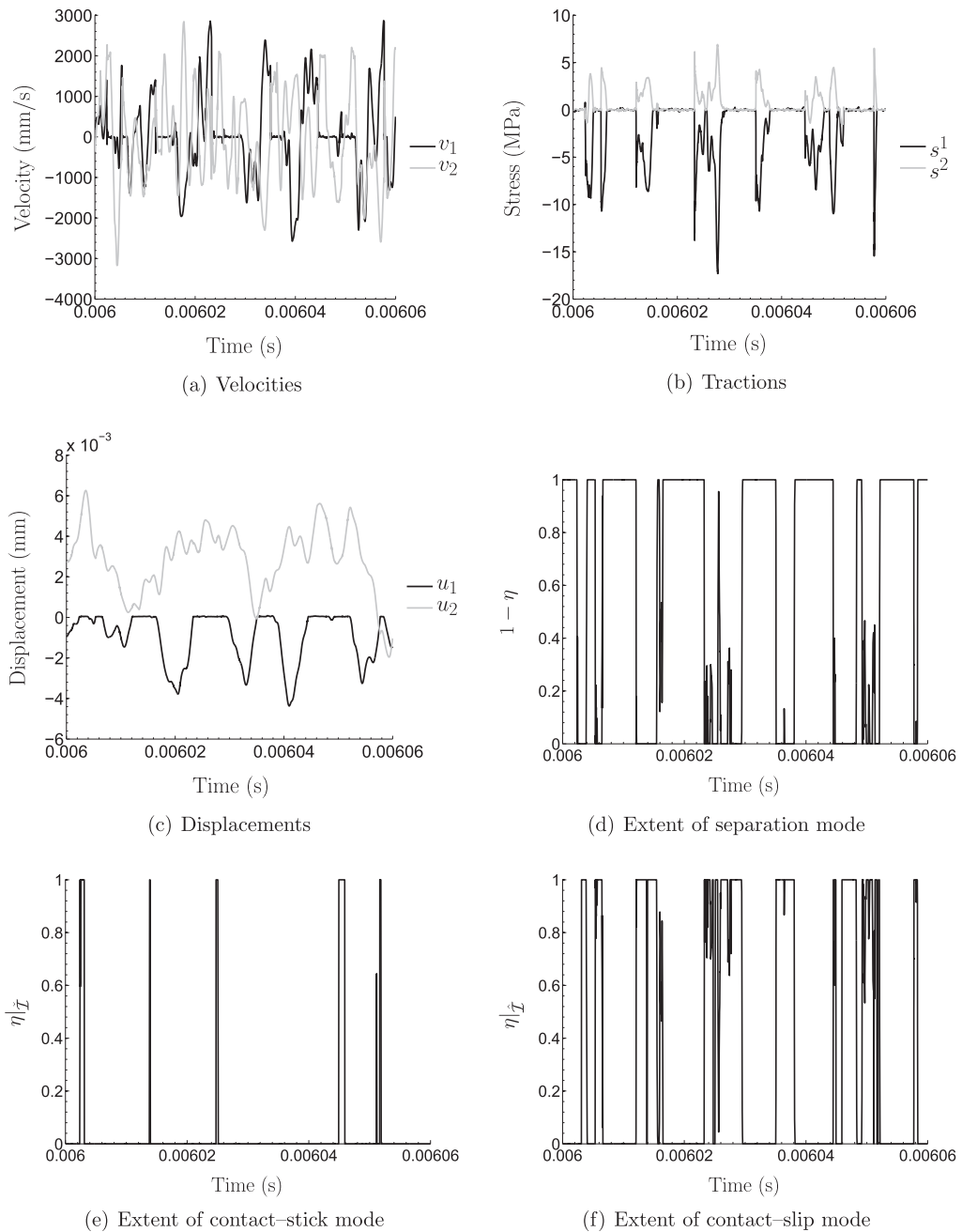


Fig. 20. Brake pad response at point A for $t \in [0.006 \text{ s}, 0.00606 \text{ s}]$.

respectively, while the corresponding values reported in [57] are about $10\sigma_0$, $2.5 \mu\text{m}$ and $5 \mu\text{m}$. Moreover, and perhaps of greater importance, our solution shows much finer detail and higher frequency oscillations, and it does not exhibit the same clear, periodic structure at later times. On the other hand, there do appear to be characteristic scales emerging in Fig. 20(d)–(f) and 21(b) and (c) that are roughly in agreement with the periodicity of the results reported in [57]. We believe that the deviations from simple periodicity in our results are due, at least in part, to the complex wave reflections from the boundaries of the pad, as described above. Since these wave interactions should continue indefinitely, we do not expect purely periodic response to develop, even for much longer durations.

We believe that differences in the resolutions of the two discrete models explain at least some of the differences in the results. The spatial discretization in [57] uses only 400 quadrilateral elements with bilinear basis functions and uniform edge lengths of $L/40$ and $H/10$. The time-marching scheme is a central difference method with a uniform step size,

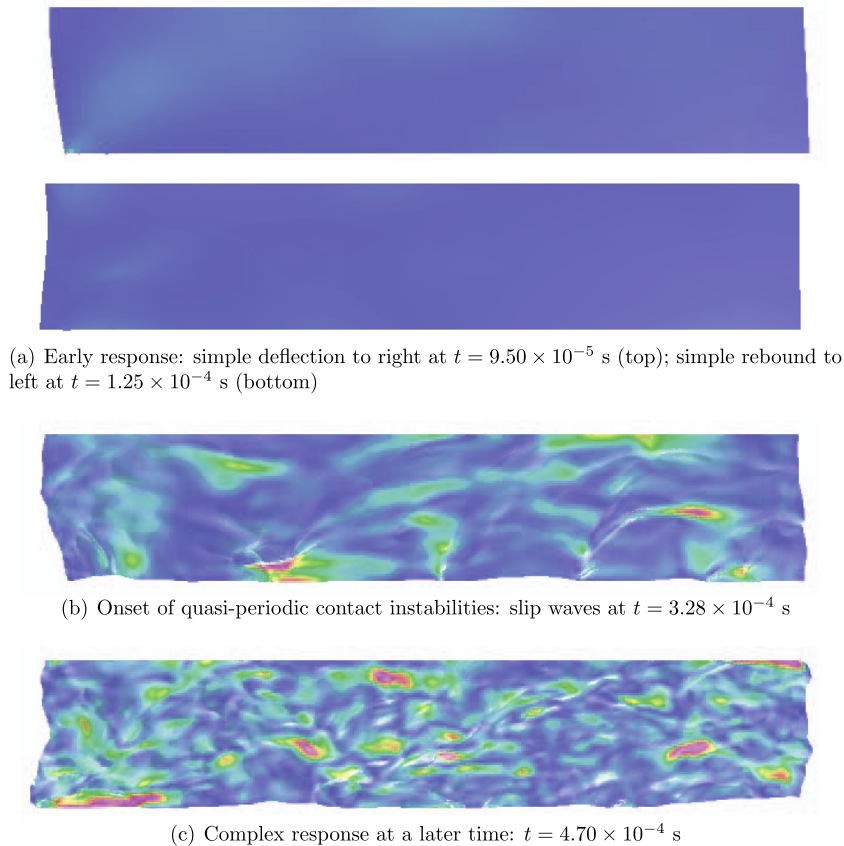


Fig. 21. Brake pad response at selected times. Deflections are scaled by a factor of 300 to reveal the pad's motion, including separation waves along its bottom edge. Color depicts strain energy density and synthetic height field depicts magnitude of the material velocity; cf. Fig. 17.

$\Delta t = 1 \times 10^{-7}$ s. Our adaptive SDG solution is much more refined. Although the initial front mesh consists of only 8 triangular elements, cf. Fig. 18, our adaptive scheme results in a strongly graded, unstructured spacetime mesh containing 900 million tetrahedral elements with complete cubic spacetime polynomial bases. The smallest spatial and temporal element diameters are about $7L \times 10^{-5}$ and $1.4L/c_d \times 10^{-5}$, respectively. These provide for much sharper resolution of wavefronts and contact-mode transitions. The numerical method in [57] relies on a special time-integration scheme [64] to produce sufficient numerical damping to suppress the spurious oscillations that would otherwise pollute the solution. This further reduces the model's resolution. Our model requires no artificial damping; the SDG formulation and the use of Riemann fluxes throughout the domain, especially the new Riemann solutions at the contact interface, eliminates the spurious oscillations without resorting to ad hoc remedies. Element-wise conservation of linear and angular momentum as well as explicit control of numerical dissipation in the adaptive spacetime meshing further limit numerical damping and preserve high-frequency detail that is likely masked in the other model.

5. Conclusions

We have presented a complete set of continuum Riemann solutions for linear elastodynamic contact and their implementation in an h -adaptive spacetime discontinuous Galerkin finite element method. In contrast to quasi-static contact formulations that are sometimes applied to dynamic models, the Riemann solutions enforce relations between the contact tractions and velocities that preserve the characteristic structure of the elastodynamic waves impinging on contact interfaces. A modified form of the contact-slip Riemann solution eliminates non-physical discontinuities at slip-stick transitions that can cause mode chatter and spurious oscillations in numerical implementations.

The SDG numerical framework offers a number of attractive features, including element-wise momentum balance, support for spatially and temporally non-uniform meshes, and a continuous mesh adaptation procedure that delivers very high-resolution solutions. As demonstrated in our previous work, weak enforcement of the proper Riemann fluxes improves accuracy and suppresses spurious oscillations in SDG solutions with sharp wavefronts. The contact Riemann solutions proposed in this work support extensions of this approach to contact problems. We obtained

near-perfect results for the reference two-bar impact problem without resorting to various algorithmic remedies that degrade accuracy in most previous numerical contact models. A regularization of separation-to-contact transitions, where discontinuous contact response is physically justified, is the only special technique in our implementation. This regularization can be arbitrarily sharp, and the analyst is afforded direct control over the maximum allowable interpenetration.

We also presented numerical results for two-dimensional examples involving impact of a square, elastic body with a rigid barrier and for the brake-pad system studied in [57]. Exact solutions are not available for these problems, but wave arrival times and the broad outline of the contact response fit expectations in the square-body impact problem. The behavior of the brake-pad system is very complex, so we are unable to perform a systematic comparison of the solutions obtained with our model and the one described in [57]. However, we observed some qualitative similarities in the solutions, including the emergence of contact instabilities and propagation of slip–separation waves along the interface between the pad and the disk. The SDG solutions show more detail, consistent with our model’s expected higher resolution. We found that the contact instabilities emit waves that traverse and reflect through the entire simulation domain. These waves have non-periodic interactions with the contact interface, so we did not observe the simple periodic response predicted for later times in [57].

Our formulation rests on a number of simplifying assumptions, as outlined in 1. Although our present results may prove useful in many practical applications, the question of whether our formulation and solution scheme are extensible to more general systems is clearly of interest. By deriving the allowable set of solutions on a material interface and applying the appropriate interface matching conditions we can obtain Riemann solutions for other friction laws and nonlinear and anisotropic material models. Efficient search algorithms that detect interpenetration or impending contact have been extensively developed elsewhere. We expect that these technologies could be combined with the adaptive capabilities of SDG meshing to relax the present assumption that knowledge of potential contact interfaces is available prior to the analysis. It might even be possible to track the evolving loci of stick–slip and contact–separation interfaces with element faces, as was done with ALE methods in [32,33], to obtain accurate solutions on coarser meshes.

Removing the restriction to isotropic friction relations is a matter of considerable practical interest. He and Curnier [48] describe sources of anisotropic surface textures that generate anisotropic frictional, including machining, wear, and anisotropic material structures. In our reformulation of the slip-mode Riemann solutions, we showed that an isotropic friction relation implies alignment of the slip velocity and the friction traction vectors. However, Riemann solutions for more generalized friction models, including the linear anisotropic friction laws developed in [48], can be obtained with the same solution strategy.

References

- [1] G.M.L. Gladwell, *Contact Problems in the Classical Theory of Elasticity*, Sijthoff & Noordhoff, 1980.
- [2] K. Johnson, *Contact Mechanics*, Cambridge University Press, Cambridge, 1985.
- [3] Z.-H. Zhong, J. Mackerle, Static contact problems – a review, *Eng. Comput.* 9 (1992) 3–37.
- [4] J. Barber, M. Ciavarella, Contact mechanics, *Int. J. Solids Struct.* 37 (2000) 29–43.
- [5] Z. Zhong, *Finite Element Procedures for Contact–Impact Problems*, Oxford University Press, Oxford, 1993.
- [6] T.A. Laursen, *Computational Contact and Impact Mechanics*, Springer, Berlin, 2002.
- [7] P. Wriggers, *Computational Contact Mechanics*, Wiley, New York, 2002.
- [8] P. Wriggers, T. Vu Van, E. Stein, Finite element formulation of large deformation impact–contact problems with friction, *Comput. Struct.* 37 (1990) 319–331.
- [9] N. Kikuchi, A smoothing technique for reduced integration penalty methods in contact problems, *Int. J. Numer. Methods Eng.* 18 (1982) 343–350.
- [10] N. Asano, A penalty function type of virtual work principle for impact contact problem of two bodies, *Bull. JSME* 29 (1986) 3701–3709.
- [11] J. Hallquist, G. Goudreau, D. Benson, Sliding interfaces with contact-impact in large-scale Lagrangian computations, *Int. J. Numer. Methods Eng.* 51 (1985) 107–137.
- [12] I. Huneke, On a penalty formulation for contact-impact problems, *Comput. Struct.* 48 (1993) 193–203.
- [13] T. Hughes, R. Taylor, J. Sackman, A. Curnier, W. Kanoknukulchai, A finite element method for a class of contact-impact problems, *Comput. Methods Appl. Mech. Eng.* 8 (1976) 249–276.
- [14] J. Simo, P. Wriggers, R. Taylor, A perturbed lagrangian formulation for the nite element solution of contact problems, *Comput. Methods Appl. Mech. Eng.* 50 (1985) 163–180.
- [15] A.B. Chaudhary, K.J. Bathe, A solution method for static and dynamic analysis of three-dimensional contact problems with friction, *Comput. Struct.* 24 (1986) 855–873.
- [16] N. Asano, Hybrid type of virtual work principle for impact contact problems of two bodies, *Bull. JSME* 29 (1986) 1679–1684.
- [17] T. Belytschko, J.I. Lin, A three-dimensional impact-penetration algorithm with erosion, *Comput. Struct.* 25 (1987) 95–104.
- [18] N.J. Carpenter, R.L. Taylor, M.G. Katona, Lagrange constraints for transient finite element surface contact, *Int. J. Numer. Methods Eng.* 32 (1991) 103–128.
- [19] J. Martins, J. Oden, A numerical analysis of a class of problems in elastodynamics with friction, *Comput. Methods Appl. Mech. Eng.* 40 (1983) 327–360.
- [20] N. Kikuchi, J.T. Oden, *Contact Problems in Elasticity: A Study of Variational Inequalities and Finite Element Methods*, SIAM, Philadelphia, 1988.
- [21] D. Sha, K. Tamma, M. Li, Robust explicit computational developments and solution strategies for impact problems involving friction, *Int. J. Numer. Methods Eng.* 39 (1996) 721–739.
- [22] A. Czekanski, S. Meguid, N. El-Abbasi, M. Refaat, On the elastodynamic solution of frictional contact problems using variational inequalities, *Int. J. Numer. Methods Eng.* 50 (2001) 611–627.
- [23] L. Jiang, R. Rogers, Combined Lagrangian multiplier and penalty function finite element technique for elastic impact analysis, *Comput. Struct.* 30 (1988) 1219–1229.
- [24] T. Laursen, V. Chawla, Design of energy conserving algorithms for frictionless dynamic contact problems, *Int. J. Numer. Methods Eng.* 40 (1997) 863–886.
- [25] F. Cirak, M. West, Decomposition contact response (DCR) for explicit finite element dynamics, *Int. J. Numer. Methods Eng.* 64 (2005) 1078–1110.
- [26] S. Lee, Rudimentary considerations for adaptive gap/friction element based on the penalty method, *Comput. Struct.* 47 (1993) 1043–1056.
- [27] L. Campos, J. Oden, N. Kikuchi, A numerical analysis of a class of contact problems with friction in elastostatics, *Comput. Methods Appl. Mech. Eng.* 34 (1981) 821–845.

- [28] G. Yagawa, H. Hirayama, A finite element method for contact problems related to fracture mechanics, *Int. J. Numer. Methods Eng.* 20 (1984) 2175–2195.
- [29] T. Belytschko, On computational methods for crashworthiness, *Comput. Struct.* 42 (1992) 271–279.
- [30] G. Li, T. Belytschko, Element-free Galerkin method for contact problems in metal forming analysis, *Eng. Comput.* 18 (2001) 62–78.
- [31] I. Zeid, J. Padovan, Finite element modeling of rolling contact, *Comput. Struct.* 14 (1981) 163–170.
- [32] R.B. Haber, J.F. Abel, Contact-slip analysis using mixed displacements, *J. Eng. Mech.* 109 (1983) 411–429.
- [33] R.B. Haber, B.H. Hariandja, An Eulerian–Lagrangian finite element approach to large-deformation frictional contact, *Comput. Struct.* 20 (1985) 193–201 (Special Issue: Advances and Trends in Structures and Dynamics).
- [34] J. Padovan, A. Kazempour, F. Tabaddor, B. Brockman, Alternative formulations of rolling contact problems, *Finite Elem. Anal. Des.* 11 (1992) 275–284.
- [35] D. Karnopp, Computer simulation of stick–slip friction in mechanical dynamic systems, *J. Dyn. Syst. Meas. Contr. Trans. ASME* 107 (1985) 100–103.
- [36] N. Mostaghel, T. Davis, Representations of Coulomb friction for dynamic analysis, *Earthquake Eng. Struct. Dyn.* 26 (1997) 541–548.
- [37] D.D. Quinn, A new regularization of Coulomb friction, *J. Vib. Acoust. Trans. ASME* 126 (2004) 391–397.
- [38] S. Meguid, A. Czekanski, Advances in computational contact mechanics, *Int. J. Mech. Mater. Des.* 4 (2008) 419–443.
- [39] L. Yin, A. Acharia, N. Sobh, R.B. Haber, D.A. Tortorelli, A spacetime discontinuous Galerkin method for elastodynamics analysis, in: B. Cockburn, G. Karniadakis, C.W. Shu (Eds.), *Discontinuous Galerkin Methods: Theory, Computation and Applications*, Springer Verlag, 2000, pp. 459–464.
- [40] R. Abedi, R.B. Haber, B. Petracovici, A spacetime discontinuous Galerkin method for elastodynamics with element-level balance of linear momentum, *Comput. Methods Appl. Mech. Eng.* 195 (2006) 3247–3273.
- [41] R.S. Falk, G.R. Richter, Explicit finite element methods for symmetric hyperbolic equations, *SIAM J. Numer. Anal.* 36 (1999) 935–952.
- [42] R. Abedi, R.B. Haber, S. Thite, J. Erickson, An h -adaptive spacetime-discontinuous Galerkin method for linearized elastodynamics, *Revue Européenne de Mécanique Numérique (Eur. J. Comput. Mech.)* 15 (2006) 619–642.
- [43] R. Abedi, M.A. Hawker, R.B. Haber, K. Matouš, An adaptive spacetime discontinuous Galerkin method for cohesive models of elastodynamic fracture, *Int. J. Numer. Methods Eng.* 1 (2009) 1–42.
- [44] S.T. Miller, B. Kraczek, R.B. Haber, D.D. Johnson, Multi-field spacetime discontinuous Galerkin methods for linearized elastodynamics, *Comput. Methods Appl. Mech. Eng.* 199 (2009) 34–47.
- [45] R. Abedi, S.H. Chung, J. Erickson, Y. Fan, M. Garland, D. Guoy, R.B. Haber, J. Sullivan, S. White, Y. Zhou, Space-time meshing with adaptive refinement and coarsening, in: *Proceedings 20th Annual ACM Symposium on Computational Geometry*, Association for Computing Machinery, 2004, pp. 300–309.
- [46] S. Thite, A unified algorithm for adaptive spacetime meshing with nonlocal cone constraints, in: *Proc. 21st European Workshop Comput. Geom. (EWCG)*, Eindhoven, Netherlands, pp. 1–4.
- [47] R. Abedi, Spacetime damage-based cohesive model for elastodynamic fracture with dynamic contact (Ph.D. thesis), Department of Theoretical and Applied Mechanics, University of Illinois at Urbana-Champaign, 2010.
- [48] Q. He, A. Curnier, Anisotropic dry friction between two orthotropic surfaces undergoing large displacements, *Eur. J. Mech. A. Solids* 12 (1993) 631–666.
- [49] S.T. Miller, R.B. Haber, A spacetime discontinuous Galerkin method for hyperbolic heat conduction, *Comput. Methods Appl. Mech. Eng.* 198 (2008) 194–209.
- [50] V.I. Arnold, *Mathematical Methods of Classical Mechanics*, second ed., Springer, New York, 1989.
- [51] A. Czekanski, S. Meguid, Analysis of dynamic frictional contact problems using variational inequalities, *Finite Elem. Anal. Des.* 37 (2001) 861–879.
- [52] W.-H. Chen, P. Tsai, Finite element analysis of elastodynamic sliding contact problems with friction, *Comput. Struct.* 22 (1986) 925–938.
- [53] F. Mahmoud, M. Hassan, N. Salamon, Dynamic contact of deformable bodies, *Comput. Struct.* 36 (1990) 169–181.
- [54] J. Solberg, P. Papadopoulos, A finite element method for contact/impact, *Finite Elem. Anal. Des.* 30 (1998) 297–311.
- [55] A. Czekanski, S. Meguid, Solution of dynamic frictional contact problems using nondifferentiable optimization, *Int. J. Mech. Sci.* 43 (2001) 1369–1386.
- [56] Y. Zhou, M. Garland, R.B. Haber, Pixel-exact rendering of spacetime finite element solutions, in: *Proceedings of IEEE Visualization 2004*, Institute of Electrical and Electronics Engineers, Inc., 2004, pp. 425–432.
- [57] L. Baillet, V. Linck, S. D'Errico, B. Laulagnet, Y. Berthier, Finite element simulation of dynamic instabilities in frictional sliding contact, *J. Tribol.* 127 (2005) 652–657.
- [58] Y. Ben-Zion, Dynamic ruptures in recent models of earthquake faults, *J. Mech. Phys. Solids* 49 (2001) 2209–2244.
- [59] S. Lykotrafitis, A. Rosakis, Sliding of frictionally held incoherent interfaces under dynamic shear loading, in: *Proceedings of the ASME/STLE International Joint Tribology Conference, IJTC 2004, Part A*, 2004, pp. 141 – 146.
- [60] G. Adams, Self-excited oscillations of two elastic half-spaces sliding with a constant coefficient of friction, *Trans. ASME J. Appl. Mech.* 62 (1995) 867–872.
- [61] G. Adams, Steady sliding of two elastic half-spaces with friction reduction due to interface stick–slip, *Trans. ASME J. Appl. Mech.* 65 (1998) 470–475.
- [62] F. Simoes, J. Martins, Instability and ill-posedness in some friction problems, *Int. J. Eng. Sci.* 36 (1998) 1265–1293.
- [63] G. Peillel, L. Baillet, Y. Berthier, Homogenization in non-linear dynamics due to frictional contact, *Int. J. Solids Struct.* 45 (2008) 2451–2469.
- [64] V. Linck, L. Baillet, Y. Berthier, Dry friction: influence of local dynamic aspect on contact pressure, kinematics and friction, in: D.D.G. Dalmaz, A.A. Lubrecht, M. Priest (Eds.), *Transient Processes in Tribology Proceedings of the 30th Leeds-Lyon Symposium on Tribology*, Tribology Series, vol. 43, Elsevier, 2004, pp. 545–552.